A Next Generation Ocean Carbon Isotope Model for Climate Studies I: Steady State Controls on Ocean ^{13}C

Mariona Claret[1] , **Rolf E. Sonnerup[1,2]**, and **Paul D. Quay[3]**

[1]Cooperative Institute for Climate, Ocean and Ecosystem Studies, University of Washington, Seattle, WA, USA, [2]NOAA Pacific Marine Environmental Laboratory, Seattle, WA, USA, [3]School of Oceanography, University of Washington, Seattle, WA, USA

Abstract The ^{13}C/^{12}C of dissolved inorganic carbon ($\delta^{13}C_{DIC}$) carries valuable information on ocean biological C-cycling, air-sea CO_2 exchange, and circulation. Paleo-reconstructions of oceanic ^{13}C from sediment cores provide key insights into past as changes in these three drivers. As a step toward full inclusion of ^{13}C in the next generation of Earth system models, we implemented ^{13}C-cycling in a 1° lateral resolution ocean-ice-biogeochemistry Geophysical Fluid Dynamics Laboratory (GFDL) model driven by Common Ocean Reference Experiment perpetual year forcing. The model improved the mean of modern $\delta^{13}C_{DIC}$ over coarser resolution GFDL-model implementations, capturing the Southern Ocean decline in surface $\delta^{13}C_{DIC}$ that propagates to the deep sea via deep water formation. Controls on $\delta^{13}C_{DIC}$ of the deep-sea are quantified using both observations and model output. The biological control is estimated from the relationship between deep-sea Pacific $\delta^{13}C_{DIC}$ and phosphate (PO_4). The $\delta^{13}C_{DIC}$:PO_4 slope from observations is revised to a value of $1.01 \pm 0.02‰$ (μmol kg^{-1})$^{-1}$, consistent with a carbon to phosphate ratio of organic matter (C:P$_{org}$) of 124 ± 10. Model output yields a lower $\delta^{13}C_{DIC}$:PO_4 than observed due to too low C:P$_{org}$. The ocean circulation impacts deep modern $\delta^{13}C_{DIC}$ in two ways, via the relative proportion of Southern Ocean and North Atlantic deep water masses, and via the preindustrial $\delta^{13}C_{DIC}$ of these water mass endmembers. The $\delta^{13}C_{DIC}$ of the endmembers ventilating the deep sea are shown to be highly sensitive to the wind speed dependence of air-sea CO_2 gas exchange. Reducing the coefficient for air-sea gas exchange following OMIP-CMIP6 protocols improves significantly surface $\delta^{13}C_{DIC}$ relative to previous gas exchange parameterizations.

1. Introduction

The ^{13}C/^{12}C of DIC ($\delta^{13}C_{DIC}$) measured during the 1990s WOCE, 2000s CLIVAR, and ongoing GO-SHIP campaigns is a relatively underutilized tool for understanding the global C-cycle. Recent decadal changes in $\delta^{13}C_{DIC}$ and the air-sea $\delta^{13}C$ disequilibrium provide high signal-noise quantification of ocean uptake and storage of anthropogenic CO_2 (Quay et al., 2007, 2017). Over longer timescales, sedimentary records of foraminiferal $\delta^{13}C$ have been used to reconstruct changes in atmospheric CO_2 and in ocean circulation (e.g., Curry & Oppo, 2005; Lisiecki, 2010, respectively). Comparisons of $\delta^{13}C$ of sedimentary planktic foraminifera with $\delta^{13}C$ of benthic foraminifera have provided reconstructions of the surface to deep contrast in $\delta^{13}C$, which have been interpreted as being caused by, for example, changes in ocean circulation and by changes in the strength of the oceanic biological pump (e.g., Duplessy et al., 1988; Hilting et al., 2008, respectively). However, there are still complications in interpreting changes in foraminiferal $\delta^{13}C$, due in part to uncertainties in the role that changes in ocean circulation can have on the whole ocean $\delta^{13}C_{DIC}$ and its surface to deep contrast, both globally and regionally (Morée et al., 2018).

One way to leverage our observations and understanding of ocean ^{13}C records is via 3-D ocean models which include isotopic fractionation during air-sea exchange and biological production (Broecker & Maier-Reimer, 1992; Holden et al., 2013; Murnane & Sarmiento, 2000; Schmittner et al., 2013; Sonnerup & Quay, 2012; Tagliabue & Bopp, 2008). For example, experiments with a coupled ocean-atmosphere model indicate that changes in Southern Ocean air-sea exchange can drive glacial-interglacial excursions in $\delta^{13}C$ of the atmosphere (Morée et al., 2018). The same model study confirms that increases in the vertical gradient in $\delta^{13}C_{DIC}$ can result from many processes: increases in biological productivity, increased particulate organic carbon sinking rates, increased nutrient uptake in the Southern Ocean, or slower gas exchange. In addition, atmospheric and oceanic $\delta^{13}C_{DIC}$ can provide information on exchange times and patterns in the terrestrial

biosphere (Keir et al., 1998; Tans et al., 1993). It is for these reasons that efforts are underway to include δ^{13}C in next-generation climate models, for example, CESM-1 (Jahn et al., 2015).

In this effort, we document an implementation of ^{13}C in the ocean component of a carbon cycling model widely used in Earth system and climate models at the National Oceanic and Atmospheric Administration's Geophysical Fluid Dynamics Laboratory (GFDL). We added ^{13}C to the carbon pools of a computationally efficient representation of ocean biological C-cycling, and to a standard air-sea gas exchange formalism for CO_2 and $^{13}CO_2$. Our new ^{13}C model corrects an isotopically heavy bias common in previous coarse resolution GFDL implementations (Sonnerup & Quay, 2012), especially at depth. Modeled $\delta^{13}C_{DIC}$ fields were analyzed using a framework to separately quantify biology, ocean circulation, and air-sea gas exchange impacts on the deep ocean mean $\delta^{13}C_{DIC}$. Applying a Redfield-based decomposition to observations and model output, we found that the ratio of $\delta^{13}C_{DIC}$ to phosphate (PO_4) is underestimated in our biogeochemical model because the fixed ratio of carbon to PO_4 in organic matter is too low. In establishing the model ocean's mean $\delta^{13}C_{DIC}$, this bias is compensated by too high PO_4 concentrations as a result of an abyssal ventilation weaker than nature. The ocean circulation influences $\delta^{13}C_{DIC}$ globally via the north versus south proportionality of deep water masses and the preindustrial sea surface $\delta^{13}C_{DIC}$ values where these waters are formed, especially in the Southern Ocean. These two factors were found to be critical in capturing the deep ocean $\delta^{13}C_{DIC}$ mean. Finally, updating the air-sea CO_2 gas exchange coefficient from that used in CMIP5 models to that implemented in the new generation of CMIP6 climate models improved the statistics of the surface $\delta^{13}C_{DIC}$ field and lowered the deep $\delta^{13}C_{DIC}$ mean by 0.15‰. The ocean model's transient response to anthropogenic ^{13}C changes will be the focus of a companion manuscript.

2. Methods

### 2.1. Global Coupled Ice-Ocean-Biogeochemistry Model

2.1.1. Physical Model

We use the ice and ocean components of the GFDL Earth System Model ESM2M (Dunne, John, et al., 2012) which is well-documented in terms of the ocean carbon cycle with different biogeochemical models (Dunne et al., 2013; Galbraith et al., 2015). It addresses key limitations in ocean circulation and air-sea exchange over a prior GFDL-based ^{13}C model (Sonnerup & Quay, 2012). Model lateral resolution is nominally 1°, enhanced meridionally to 1/3° in the tropics, and the vertical resolution is 10 m in the upper 220 m, decreasing gradually to 370 m in the abyss for a total of 50 layers, a major improvement in spatial resolution compared to previous ocean-^{13}C models (Schmittner et al., 2013; Sonnerup & Quay, 2012; Tagliabue & Bopp, 2008).

In order to reduce computational cost associated with the ^{13}C long equilibration time ($\sim$5,000 years), the atmosphere and land are not coupled to the ocean, as they are in ESM2M. Instead, prescribed atmospheric forcing (Large & Yeager, 2004) and runoff (Dai et al., 2009) are used from the repeating annual cycle of the Common Ocean Reference Experiment version 2 Normal Year Forcing data set (COREv2-NYF). To implement this forcing, the ice-ocean coupled model here differs from that in ESM2M in the following ways: First, the ocean model MOM4p1 is updated to version 5.1 (MOM5, Griffies, 2012a). Second, the atmospheric forcing implementation follows the Coordinated Ocean-ice Reference Experiments (CORE) protocol (Griffies et al., 2009) revised for MOM5 (Griffies, 2012b), according to which the ocean is forced with air-sea fluxes using bulk formulas and surface salinity is restored with salt fluxes. In addition, ocean surface albedo is prescribed as a function of latitude as in CM2.1-CORE (Griffies, 2012b) and is not treated differently in terms of direct and diffusive shortwave radiation as it would be in ESM2M with a coupled atmosphere.

2.1.2. Biogeochemical Model with ^{13}C

We use the Biogeochemistry with Light Iron Nutrients and Gas (BLING, Galbraith et al., 2010) model as it reproduces key aspects of the ocean carbon cycle at minimal computational cost (Galbraith et al., 2015). BLING simulates the biogeochemical cycle of four prognostic core tracers: dissolved inorganic (PO_4) and organic (DOP) phosphate, dissolved oxygen (O_2), and dissolved iron (Fe). As PO_4 is the macronutrient, nitrogen fixation and denitrification are not included in BLING. The carbon cycle builds upon phosphate via elemental Redfield ratios and two prognostic tracers: dissolved inorganic carbon (DIC) and alkalinity (ALK; Bernardello et al., 2014). Air-sea exchanges for oxygen and carbon follow the Ocean Carbon Model
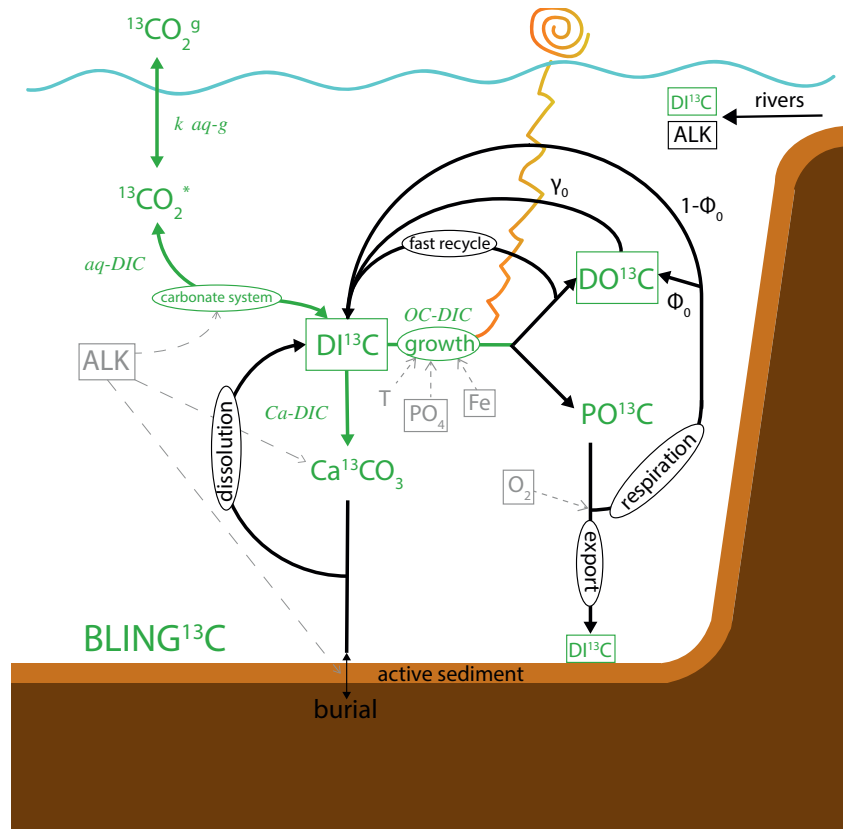
Figure 1. Schematics of ^{13}C-cycle coupled to BLING. Pathways to which an isotopic fractionation α is applied are shown in green; while those that are only a function of R_{DIC} are shown in black. See Appendix A for notation and formulation of isotopic fractionations denoted. Complex pathways are enclosed in circles (see Galbraith et al., 2010 for a full description) and their dependencies on temperature (T) and other biogeochemical tracers are shown in gray dashed lines. Prognostics tracers are enclosed in squares, while those not enclosed are implicit in the model meaning that their fluxes are diagnosed considering an ecosystem in steady state. BLING, Biogeochemistry with Light Iron Nutrients and Gas; DIC, dissolved inorganic carbon.

Intercomparison Project (OCMIP2) protocol (Najjar & Orr, 1998) using Schmidt numbers for the computation of gas exchange piston velocities from ESM2M (Dunne et al., 2013), revised from Wanninkhof (1992). Carbon burial into the bottom sediment layer follows Dunne, Hales, et al. (2012). BLING is embedded in the ice-ocean coupled model providing tracer tendency terms from biogeochemical sources and sinks and a chlorophyll field for the attenuation of shortwave radiation, while the physical model advects and mixes BLING prognostic tracers within the ocean and computes air-sea gas exchange fluxes for CO_2 and O_2.

The cycling of carbon-13 (^{13}C) is included in BLING (hereinafter called BLING^{13}C) by (i) adding two prognostic tracers, dissolved inorganic (DI^{13}C) and labile dissolved organic (DO^{13}C) carbon-13, (ii) diagnosing particulate organic carbon-13 (PO^{13}C) and ^{13}C calcium carbonate (Ca^{13}CO$_3$) fluxes, and (iii) applying isotopic fractionations to air-sea CO_2 gas exchange and to the production of organic matter and calcium carbonate. A description of BLING^{13}C is provided below, a schematic in Figure 1, and detailed formulation of isotopic fractionations in Appendix A. It is noted that in BLING^{13}C the DI^{12}C concentration is approximated as DIC which is a common practice in conventional ocean biogeochemical models that do not carry a separate DI^{12}C tracer (see Schmittner et al., 2013). This approximation implies that the computation of δ^{13}C of DIC ($\delta^{13}C_{DIC}$) in BLING^{13}C needs to use the ratio of DI^{13}C to DIC (R_{DIC}) in agreement with the ^{13}C model formulation. This contrasts with the $\delta^{13}C_{DIC}$ definition which uses the ratio of DI^{13}C to DI^{12}C (see Appendix B for a reconciliation between the two definitions).

Isotopic fractionation of ^{13}C during air-sea gas exchange and photosynthetic production of organic matter (OM) is implemented as in Schmittner et al. (2013), with fractionations during carbon speciation and air-sea
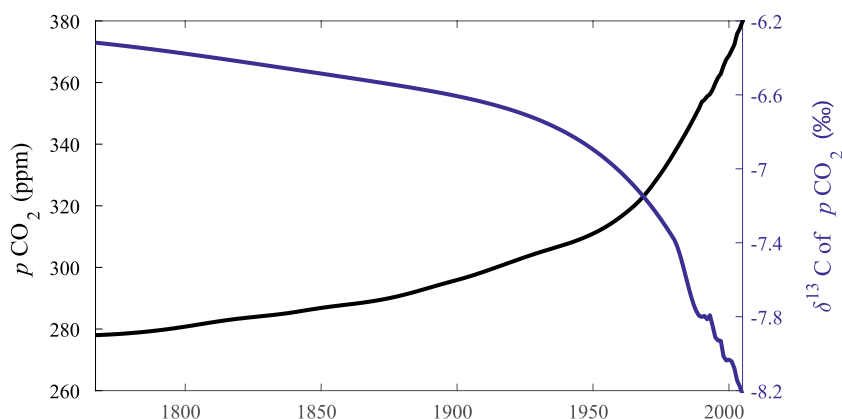
Figure 2. Atmospheric timeseries of $p\mathrm{CO_2}$ and $\delta^{13}\mathrm{C}$ of $p\mathrm{CO_2}$ implemented in the industrial era simulation.

exchange from Zhang et al. (1995), and fractionation during OM formation dependent on $p\mathrm{CO_2}$ based on Popp et al. (1989). The production of $^{13}\mathrm{C}$ OM is partitioned into dissolved and particulate organic pools with the same $^{13}\mathrm{C}/^{12}\mathrm{C}$ composition (hereinafter referred as $\delta^{13}\mathrm{C_{org}}$) using the empirical parameterization of the ratio between particulate export and primary production of Dunne et al. (2005) implemented in BLING. The resulting $^{13}\mathrm{C}$ particle flux is instantaneously redistributed over the water column following a sinking and remineralization profile that lies between the classic Martin curve and that used in OCMIP2 (Galbraith et al., 2010). Finally, a 1‰ fractionation is applied to the formation of $\mathrm{Ca^{13}CO_3}$ while none it is applied to its dissolution. At the sea floor, a $\mathrm{Ca^{13}CO_3}$ burial flux is included weighting the calcium carbonate burial flux by the $\delta^{13}\mathrm{C}$ content of the active sediment layer, which is diagnosed.

2.1.3. Preindustrial and Industrial-Era Simulations

BLING^{13}C, coupled to the ice-ocean physical configuration of MOM5.1 (hereinafter MOM5-BLING^{13}C), was run in two stages. First, a spin up of about 6,000 years was required to equilibrate the ocean carbon chemistry with preindustrial atmospheric $\mathrm{CO_2}$ and $^{13}\mathrm{CO_2}$ levels of $p\mathrm{CO_2}$ = 278 ppm and $\delta^{13}\mathrm{C}$ of -6.28‰ (Francey et al., 1999). The model's physical state was initialized using an earlier ESM2M spin up for the ocean hydrography, without sea ice, and with the ocean at rest. The biogeochemistry was initialized from an earlier preindustrial spin up of ESM2M coupled to BLING (Galbraith et al., 2015). For $^{13}\mathrm{C}$ initial conditions, we used output from a coarse resolution GFDL model spun up to steady state ("LoLo" in Sonnerup & Quay, 2012, hereinafter MOM3-OCMIP-LoLo). At the end of the C-cycle spin up, the ocean physics was in steady state, while the carbon biogeochemistry was still not fully in equilibrium due to the long timescale of the calcite burial. The small drift in carbon, however, had a small impact on $\delta^{13}\mathrm{C_{DIC}}$, which reached nearly equilibrium with a preindustrial volume-averaged global $\delta^{13}\mathrm{C_{DIC}}$ of 0.58‰ and surface mean $\delta^{13}\mathrm{C_{DIC}}$ of 2.24‰. See Appendix C for a full evaluation of the physical and biogeochemical ocean states at the end of the spin up.

The second stage, starting from the preindustrial state, involved two 235-years long simulations. The first simulation maintained preindustrial atmospheric $\mathrm{CO_2}$ and $^{13}\mathrm{CO_2}$ levels, while the second one was forced by a historical time series of $p\mathrm{CO_2}$ and $p^{13}\mathrm{CO_2}$. This time series spanned from 1768 to 2002 using an updated compilation of ice core and firn $\mathrm{CO_2}$ measurements (Francey et al., 1999) amended with contemporary $^{13}\mathrm{CO_2}$ observations of the global atmosphere collected at Point Barrow, Mace Head, Mauna Loa, Christmas Island, Samoa, Cape Grim, and South Pole observatories (Figure 2). The anthropogenic perturbation was computed from the difference between these two simulations.

In all MOM5-BLING^{13}C runs, a riverine carbon flux input of 0.45 Gt C yr^{-1} (Jacobson et al., 2007; Sarmiento & Sundquist, 1992) was distributed equally among rivers with a concentration of 9.75×10^{-4} mol kg^{-1} and a $\delta^{13}\mathrm{C_{DIC}}$ signature of -27.3‰ ($\sim$21‰ depleted relative to preindustrial atmospheric $\mathrm{CO_2}$ (Tans et al., 1993). To offset the change in pH from the DIC flux, that could affect air-sea fluxes in river plumes, we also added a constant ALK concentration of 1.0725×10^{-3} eq kg^{-1}.

Table 1

$\delta^{13}C_{DIC}$ Statistics Over a Variety of Models

Model	Surface $\delta^{13}C_{DIC}$			Interior $\delta^{13}C_{DIC}$		
	Mean	R	NRMSE	Mean	R	NRMSE
MOM5-BLING[13]C-*std*	1.57	0.58	0.92	(0.24)	(0.91)	(0.47)
MOM5-BLING[13]C-*fast*	1.51	0.45	1.14	(0.38)	(0.90)	(0.48)
MOM3-OCMIP-LoLo[1]	1.66	0.37	1.09	(0.90)	(0.80)	(0.61)
MOM3-OCMIP-HiHi[1]	2.49	0.34	1.02	(1.11)	(0.88)	(0.50)
ORCA2-PISCES-C[2]	1.8	0.41	0.70	1.10	0.74	0.55
ORCA2-PISCES-D[2]	1.7	0.44	0.50	1.00	0.65	0.77
UVic-2.8-std[3]	1.7	0.49	1.19	0.59	0.85	0.58
UVic-2.8-FeL[3]	1.6	0.53	0.99	0.59	0.88	0.50
Observations	1.5			0.34 ± 0.38 (0.35 ± 0.39)[4]		

Interior $\delta^{13}C_{DIC}$ is below 1 km depth. Parenthesis are volume-weighted statistics that use the same land masking. Observational interior $\delta^{13}C_{DIC}$ mean and standard deviation are computed by previously binning GLODAPv2.2020 data into $1° \times 1° \times 500$ m cells below 1 km south of 60°N to exclude the Arctic.

Abbreviations: BLING, Biogeochemistry with Light Iron Nutrients and Gas; DIC, dissolved inorganic carbon; OCMIP, Ocean Carbon Model Intercomparison Project.

[1]Sonnerup and Quay (2012). [2]Tagliabue and Bopp (2008). [3]Schmittner et al. (2013). [4]Eide, Olsen, Ninnemann, and Johannessen (2017).

The sensitivity of the simulation to air-sea CO_2 gas exchange was tested by repeating preindustrial and industrial era simulations using the OMIP-CMIP6 protocol for air-sea gas exchanges (Orr et al., 2017) instead of the OCMIP2 one. For CO_2 this implied the modification of the gas transfer coefficient k_0 and the Schmidt number Sc in the equation for the piston velocity k, namely

$$k = k_0 \left(1 - s\right) u^2 \sqrt{660 / Sc}, \tag{1}$$

where s is the sea ice cover and u the wind speed 10 m above sea level. Specifically, we changed k_0 from 0.337 (OCMIP2) to 0.251 (OMIP-CMIP6) and updated the coefficients for the Schmidt number computation accordingly. By convention, k and u are in units of cm hr^{-1} and m s^{-1}, respectively, so that k_0 has units of (cm hr^{-1})/(m s^{-1})^2 given that s and Sc are dimensionless numbers. The simulation using the OMIP-CMIP6 protocol was initialized with the steady state condition resulting from that using the OCMIP2 protocol and spin up for 3,000 years with preindustrial atmospheric carbon levels -running another 6,000 years spin up was beyond our computational resources. After 3,000 years, the CO_2 transient scenario was run in two branches, as described in the case using the OCMIP2 protocol. At the end of the spin up, surface and global $\delta^{13}C_{DIC}$ means were not fully in steady state (see Appendix C). However, the model bias of contemporary surface $\delta^{13}C_{DIC}$ is less than 0.1‰, an improvement relative to previous ^{13}C-cycling models (Table 1), and the global $\delta^{13}C_{DIC}$ mean is about 0.12‰ lighter than obtained using the OCMIP2 with a longer spinup, which is about the difference reported by Schmittner et al. (2013) (0.1‰) when shifting from $k_0 = 0.337$ to $k_0 = 0.251$ running longer spin up simulations. Hereinafter, the pair of simulations using the OMIP-CMIP6 protocol are referred as *standard* since the 0.251 k_0 value is in closer agreement with recent air-sea CO_2 gas parameterizations (Nigthtingale et al., 2000; Ho et al., 2006; Sweeney et al., 2007; Wanninkhof, 2014). The pair of simulations that use the OCMIP2 protocol with an increased k_0 value close to that of Wanninkhof (1992) are instead referred as *fast-gas-exchange*.

2.2. Data to Model Comparison

To evaluate MOM5-BLING[13]C, we use a variety of data sets. At the sea surface, we use a comprehensive data set normalized to year 1995 to correct for temporal changes in ^{13}C due to ocean uptake of anthropogenic CO_2. This normalization removes the surface ^{13}C Suess effect between the year of collection and 1995 for each measurement using meridional trends of anthropogenic $\delta^{13}C_{DIC}$ accumulation rates since the 1970s that are basin specific (Quay et al., 2003). At depth, the modeled global ocean $\delta^{13}C_{DIC}$ field is compared to

the modern $\delta^{13}C_{DIC}$ gridded climatology of Eide, Olsen, Ninnemann, and Johannessen (2017). This product is built by mapping separately, and adding later, the ^{13}C Suess effect and preindustrial $\delta^{13}C_{DIC}$ into $1° \times 1°$ grid maps using WOA09 and GLODAPv1.1 annual climatologies. The former mapping uses Multiple Linear Regressions (MLRs) of the ^{13}C Suess effect fit to pCFC-12. The later mapping uses MLRs of $\delta^{13}C_{DIC}$ corrected for the Suess effect fit to observed temperature, salinity, PO_4, and apparent oxygen utilization. The resulting modern $\delta^{13}C_{DIC}$ climatology provides two advantages over direct $\delta^{13}C_{DIC}$ measurements from GLODAP: First, it has undergone secondary quality-control, and second, it is gridded, so we can compute volume-weighted statistics. This data set is compared with model output between 1991 and 1998 since this period comprises 90% of the cruises used to construct Eide's MLRs (see Table 1 in Eide, Olsen, Ninnemann, and Eldevik (2017)). For stoichiometric analyses at depth, for example, $\delta^{13}C_{DIC}$ versus PO_4 as in Section 3.2, we used in-situ values from the GLODAPv2.2020 data product (Olsen et al., 2020) since it offers $\delta^{13}C_{DIC}$ point data that are synoptic with and not computed from other biogeochemical properties, and it includes $\delta^{13}C_{DIC}$ data corrections in the North Atlantic over previous GLODAP versions (Becker et al., 2016). These point data are compared with model output over the 1990–2002 time period because the atmospheric $\delta^{13}C$ of pCO$_2$ time series used to force the ocean biogeochemistry does not extend beyond that period. We have not limited GLODAPv2.2020 data to year 2002 as this did not significantly impact our results yet reduced the spatial coverage available as the number of observations was halved. For organic matter, its modeled $^{13}C/^{12}C$ content ($\delta^{13}C_{org}$) is compared to $\delta^{13}C$ of particulate organic carbon ($\delta^{13}C_{POC}$) data compiled by Goericke and Fry (1994) within the mixed layer. Modeled $\delta^{13}C_{org}$ is analyzed for the 1968–1993 time period, when observations were collected, and over the mixed layer.

Finally, it is noted that seasonal variability of $\delta^{13}C_{DIC}$ can introduce aliasing effects in the model comparison with observations specially at high latitudes such as in the North Atlantic, where the seasonal surface $\delta^{13}C_{DIC}$ range is about 1‰ (Becker et al., 2018) and observations are biased toward summer months. In order to minimize this effect, MOM5-BLING^{13}C modeled fields of $\delta^{13}C_{DIC}$ and $\delta^{13}C_{org}$ are weighted by the seasonal distribution of the observations to which model output is compared over the time periods above mentioned. The seasonal distributions of surface and subsurface $\delta^{13}C_{DIC}$ are computed over 20° latitude bands between 80°S and 80°N in each basin (Figure S1). To infer the seasonal distribution of Eide's grid product, we have used GLODAPv2.2020 data between 1990 and 2000. In contrast, the seasonal distribution of $\delta^{13}C_{org}$ is less diverse, dominated by spring (April–June) sampling in the Pacific and Indian Oceans (north of 40°S), by winter sampling (January–March) in the Southern Ocean (south of 40°S), by October sampling in the South Atlantic, and by July sampling in the North Atlantic. Below 2,000 m, point data is not weighted since at these depths the modeled seasonal variability is about one order of magnitude smaller than meridional gradients across basins. Modeled fields from the coarse resolution GFDL-MOM3 are not seasonally weighted as only annually averaged fields are available.

3. Results and Discussion

3.1. Model Evaluation of Contemporary ^{13}C Tracer Fields

3.1.1. Surface Ocean

The *standard* simulation of MOM5-BLING^{13}C (hereinafter MOM5-BLING^{13}C-*std*) captures well the meridional patterns observed in surface $\delta^{13}C$ of DIC ($\delta^{13}C_{DIC}$) at year 1995, higher values in the tropics and at high latitudes, and relatively low values in the subtropical gyres and at the Equator (Figures 3a and 3b). In the Southern Ocean, MOM5-BLING^{13}C-*std* reproduces the $\delta^{13}C_{DIC}$ peak near 45°S and the sharp decline in $\delta^{13}C_{DIC}$ poleward of 50°S, a feature that was absent in the prior GFDL-based, relatively coarse resolution ($4.5° \times 4° \times 24$ levels) model MOM3-OCMIP-LoLo (Figures 3c and 3d). Enhanced grid and bathymetric resolution and improved ocean mixing parameterizations specific to ESM2M, on which our ice-ocean coupled model is based, likely play a role in this regard. MOM5-BLING^{13}C-*std* also resolves the isotopically light tongue in the Equatorial Pacific that was missing in MOM3-OCMIP-LoLo (see discrepancy between blue lines in the Equator in Figure 3d). With increased vertical resolution in MOM5-BLING^{13}C-*std*, the equatorial upwelling is stronger and from shallower, more realistic depths (Toggweiler et al., 1989).

The model bias (0.07‰) of surface $\delta^{13}C_{DIC}$ in MOM5-BLING^{13}C-*std* is comparable to laboratory intercalibration accuracy ($\pm 0.1 - 0.2$‰, see Appendix A in Schmittner et al., 2013), and about half that of the
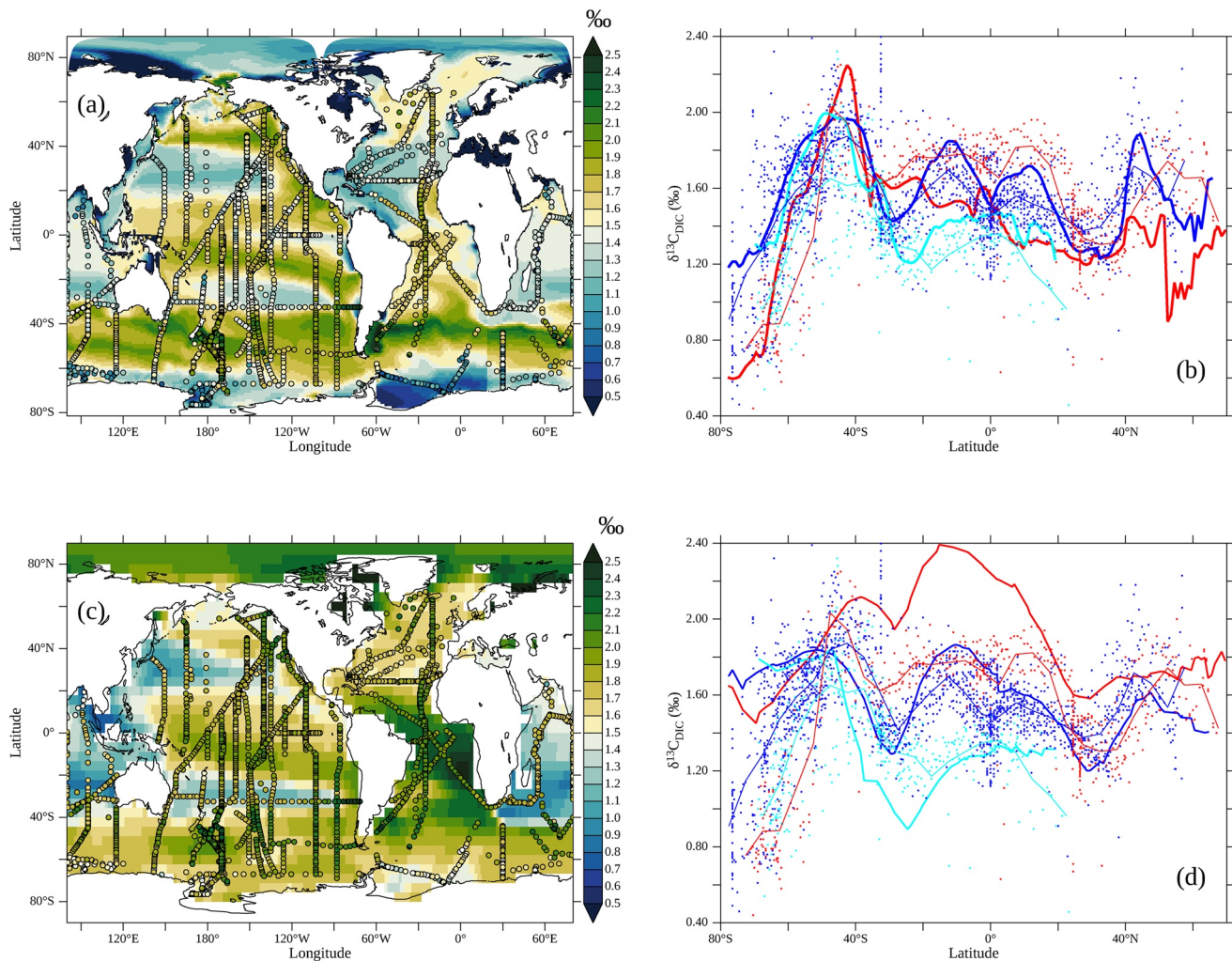
Figure 3. (a) Surface $\delta^{13}C_{DIC}$ field in MOM5-BLING^{13}C-*std* (in ‰ units) at year 1995 overlaid with observational data normalized to the same year (filled circles, Sonnerup & Quay, 2012). (b) Meridional plots of the zonally averaged modeled surface field shown in (a) for each basin (thick solid lines). Observations normalized to year 1995 are shown as both point data (crosses) and zonal averages over 5° latitude bins (thin solid lines) for better visualization. Color code corresponds to the Atlantic Ocean (red), Pacific Ocean (blue), and Indian Ocean (cyan). (c),(d) As (a),(b) but for model MOM3-OCMIP-LoLo. $\delta^{13}C_{DIC}$ in MOM3-OCMIP-LoLo has been adjusted downward by 0.2‰ to account for the the effect of riverine organic matter on the oceanic $\delta^{13}C$ (Sonnerup & Quay, 2012). BLING, Biogeochemistry with Light Iron Nutrients and Gas; OCMIP, Ocean Carbon Model Intercomparison Project.

coarse resolution MOM3-OCMIP-LoLo model (∼0.16‰, Figure 4). The modeled surface ^{13}C Suess effect global average is −0.14‰ over an atmospheric ^{13}C Suess effect of about −0.64‰ (between the 1990s and the 1970s), 0.02‰ weaker than the observed surface ^{13}C Suess effect over the same time period (−0.16‰, Quay et al., 2003). Scaling this model bias to the full ^{13}C Suess effect between the 1990s and the preindustrial year 1768, a change in atmospheric $\delta^{13}C$ of pCO_2 of −1.63‰, gives 0.09‰, which could explain the general bias in modeled surface $\delta^{13}C_{DIC}$. The correlation coefficient R between modeled and observed surface patterns is $R = 0.58$ which is a marked improvement relative to MOM3-OCMIP models, whose R values range from 0.3 to 0.4 (Table 1). MOM5-BLING^{13}C-*std* output is closest to observations along with model UVic-2.8-FeL (Table 1). However, quantitative comparison between models (other than MOM3 and MOM5) is hindered by the fact that different observational datasets were used.

Among basins, the Southern Ocean (defined as south of 58°S), Indian and Pacific's surface $\delta^{13}C_{DIC}$ are mostly unbiased, while the Atlantic Ocean north of 40°S is biased significantly low (Figure 4). The bias in the Atlantic Ocean may be due to local input of riverine organic matter with too low $\delta^{13}C$. Riverine organic matter plumes, especially from the Amazon and Congo rivers, are entrained into the large-scale circula-
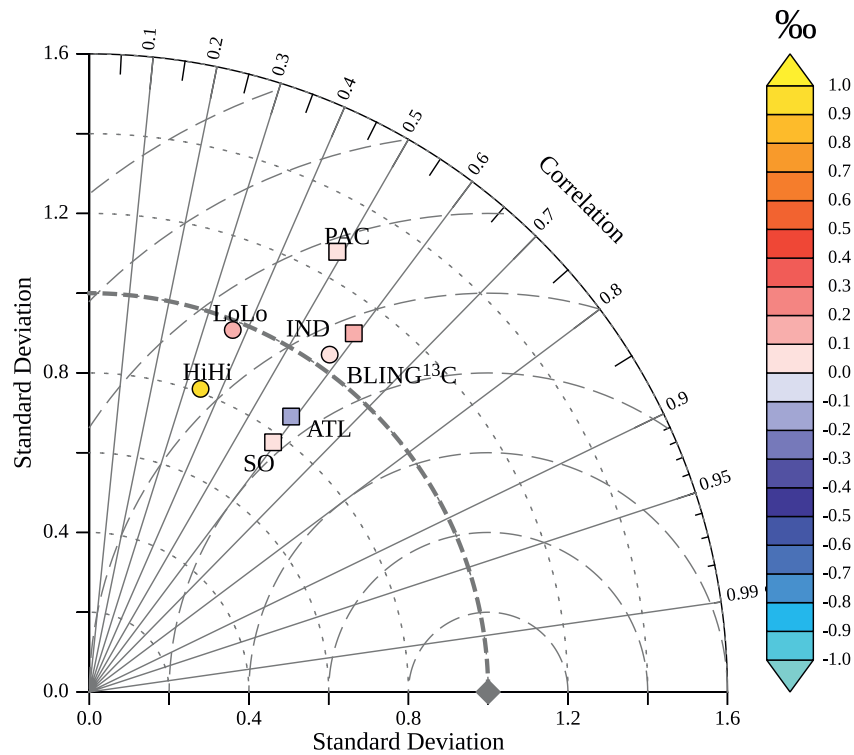
Figure 4. Taylor diagram of modeled surface $\delta^{13}C_{DIC}$ with MOM5-BLING^{13}C-*std* (BLING^{13}C), MOM3-OCMIP-LoLo (LoLo), and MOM3-OCMIP-HiHi (HiHi) for the climatology of Eide, Olsen, Ninnemann, and Johannessen ([2017](#)). Circles are statistical values for the global ocean $\delta^{13}C_{DIC}$, while squares are for each ocean basin (Atlantic, ATL; Pacific, PAC, Indian, IND, Southern Ocean, SO). The correlation coefficient is the azimuthal angle (solid lines), the modeled standard deviation is normalized by that of the observations (dotted lines), and the root mean square (RMS) difference is shown through two components, the overall model bias (filled color in units of ‰) and the centered RMS error normalized by the observed standard deviation (NRMSE, dashed lines). The NRMSE is zero at the gray diamond and increases by 0.2 along concentric circles away from it. All statistics are volume-weighted. MOM3-OCMIP-LoLo and MOM3-OCMIP-HiHi values have been corrected for the effect of riverine organic matter on $\delta^{13}C_{DIC}$ as in Figure [3](#). Masking and regridding modeled and observed $\delta^{13}C_{DIC}$ fields to a unique grid for comparison with observations introduces an error of about ±0.02‰. BLING, Biogeochemistry with Light Iron Nutrients and Gas; OCMIP, Ocean Carbon Model Intercomparison Project; RMS, root mean square.

tion exerting an outsize influence on the open Atlantic ocean (e.g., Muller-Karger et al., [1988](#)). A riverine $\delta^{13}C_{DIC}$ content of −14‰, as found in the Amazon river (Quay et al., [1992](#)), would increase surface $\delta^{13}C_{DIC}$ in the North Atlantic by about 0.25‰, relative to the −27‰ content used here, for a riverine DIC input of 0.14 Pg C yr^{-1} and a preindustrial gross CO_2 exchange flux of 7.28 Pg C yr^{-1} (north of 20°S and between 75°W and 0°). Although Sonnerup and Quay ([2012](#)) noted that inter-basin trends in $\delta^{13}C_{DIC}$ are sensitive to the model's overall rate of overturning, their models did not include riverine organic carbon fluxes. Another explanation could be a stronger modeled surface ^{13}C Suess effect than in nature. However, the change in surface $\delta^{13}C_{DIC}$ between the early 1980s (1981–1983) and the early 1990s (1992–1995) north of 10°S and south of 65°N is smaller than observed over the same time period and area (−0.16‰ vs. −0.19‰ Quay et al., [2003](#)), which would drive a higher -instead of lower- surface $\delta^{13}C_{DIC}$ in the model. Therefore, our results indicate that the details of where riverine fluxes enter the ocean may be a significant driver of the inter-basin trends in $\delta^{13}C_{DIC}$.

The biological fractionation implemented in MOM5-BLING^{13}C-*std* is governed only by aqueous pCO$_2$, and modeled aqueous CO_2 agrees well, specially at low and mid latitudes, with that compiled by Goericke and Fry ([1994](#)) (Figure S2), which is contemporaneous and spatially consistent with their $\delta^{13}C_{POC}$ compilation. The model captures the meridional trend of $\delta^{13}C_{POC}$ compiled by Goericke and Fry ([1994](#)) (Figure [5](#)), which increases toward the Equator as pCO$_2$ decreases. The modeled $\delta^{13}C_{org}$ tends to be too low north of 40°N, and misses the high $\delta^{13}C_{org}$ values at 42°S in the Indian Ocean and at 10°S nearby the Eastern coast of the Pacific
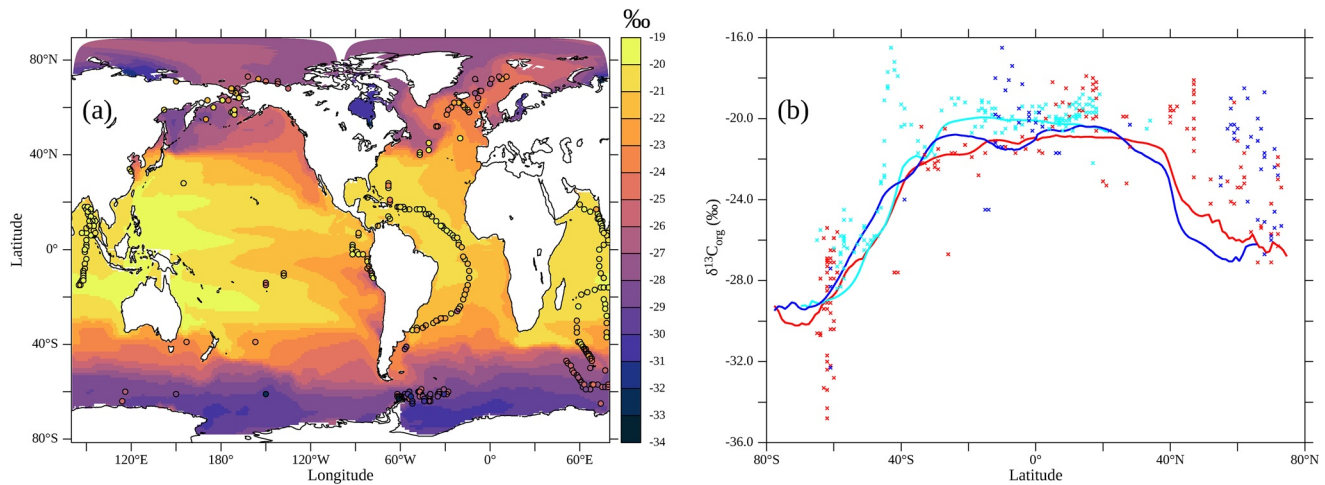
Figure 5. As in Figures 3a and 3b but for $\delta^{13}C$ of organic matter ($\delta^{13}C_{org}$) in units of ‰. Modeled values are mixed-layer averaged in MOM5-BLING^{13}C-*std* and observed values correspond to the data set of Goericke and Fry (1994) within the mixed layer. BLING, Biogeochemistry with Light Iron Nutrients and Gas.

Ocean where few data exist. Model-data mismatches are likely due to ignoring biological process affecting $\delta^{13}C_{org}$ including the dependency of $\delta^{13}C_{org}$ on the CO_2 fixation rate (Laws et al., 1995) and the influence of cell surface area and permeability to the phytoplankton interior (Keller & Morel, 1999). Inaccuracies in simulating $\delta^{13}C_{org}$ could contribute to the $\delta^{13}C_{DIC}$ bias in the Southern Ocean, mid latitudes of the North Atlantic, and in the South Atlantic. However, discrepancies between modeled and observed $\delta^{13}C_{org}$ do not explain the model-data $\delta^{13}C_{DIC}$ mismatch in the tropical North Atlantic and near the Peruvian upwelling: an isotopically lighter $\delta^{13}C_{org}$ would translate into an isotopically heavier $\delta^{13}C_{DIC}$, while the opposite is found (Figures 3a and 5a).

3.1.2. Subsurface Ocean

Modeled subsurface $\delta^{13}C_{DIC}$ agrees well with the climatology of Eide, Olsen, Ninnemann, and Johannessen (2017) for the 1990s (Figures 6a–6f). MOM5-BLING^{13}C-*std* captures the low $\delta^{13}C_{DIC}$ tongue of older waters in the Indian and Pacific Oceans and the meridional $\delta^{13}C_{DIC}$ trends in the Atlantic, although $\delta^{13}C_{DIC}$ is too low in the Southern Ocean. In contrast, the deep ocean $\delta^{13}C_{DIC}$ MOM3-OCMIP-LoLo is significantly high (Figures 6g–6i). The Atlantic Ocean circulation may play a key role in this regard, as it is where the two primary deep waters are formed, the Southern Ocean Deep Water (SODW) and the North Atlantic Deep Water (NADW). In salinity versus $\delta^{13}C_{DIC}$ plots, the two distinct deep waters define two extrema. Deep water sources in MOM3-OCMIP-LoLo are isotopically heavier than in MOM5-BLING^{13}C-*std* and observations (Figure 7) after correcting for the absence of riverine inputs in the coarse resolution model (globally about −0.2‰, Sonnerup & Quay, 2012; Tans et al., 1993).

The global $\delta^{13}C_{DIC}$ field of deep waters (below 1 km) in MOM5-BLING^{13}C-*std* is improved relative to MOM3-OCMIP-LoLo with a decreased model bias (−0.11‰ vs. 0.55‰ in MOM3) and a higher correlation coefficient ($R = 0.91$ vs. $R = 0.8$–0.88 for MOM3) (Figure 8a). The −0.11‰ bias in MOM5-BLING^{13}C-*std* is unlikely to be driven by a bias in the oceanic ^{13}C Suess effect as the modeled depth-integrated $\delta^{13}C_{DIC}$ change between 1990 and 1970 (−61.7‰ m decade^{-1}) is slightly smaller than the observed one over the same period (−65 ± 33‰ m decade^{-1}, Quay et al., 2003). A full evaluation on the drivers underlying this bias is given in Section 3.2. Compared to other models with ^{13}C cycling, MOM5-BLING^{13}C-*std* performs similarly to the UVic-2.8 model (Schmittner et al., 2013) in the sense that it significantly reduces a high bias in subsurface $\delta^{13}C_{DIC}$ that is common in ocean ^{13}C models (Table 1).

Although global model bias is low, the correlation coefficient is poor in the Southern Ocean (Figure 8b). The vertical $\delta^{13}C_{DIC}$ gradient is set at the surface by air-sea gas exchange and biological production, which both increase $\delta^{13}C_{DIC}$ at high latitudes, and below the mixed layer by remineralization of organic matter, which decreases $\delta^{13}C_{DIC}$. This gradient is then smoothed by vertical ocean mixing. In the Southern Ocean, modeled $\delta^{13}C_{DIC}$ is more homogeneous than observed (Figures 6d–6f), which may be indicative of overly
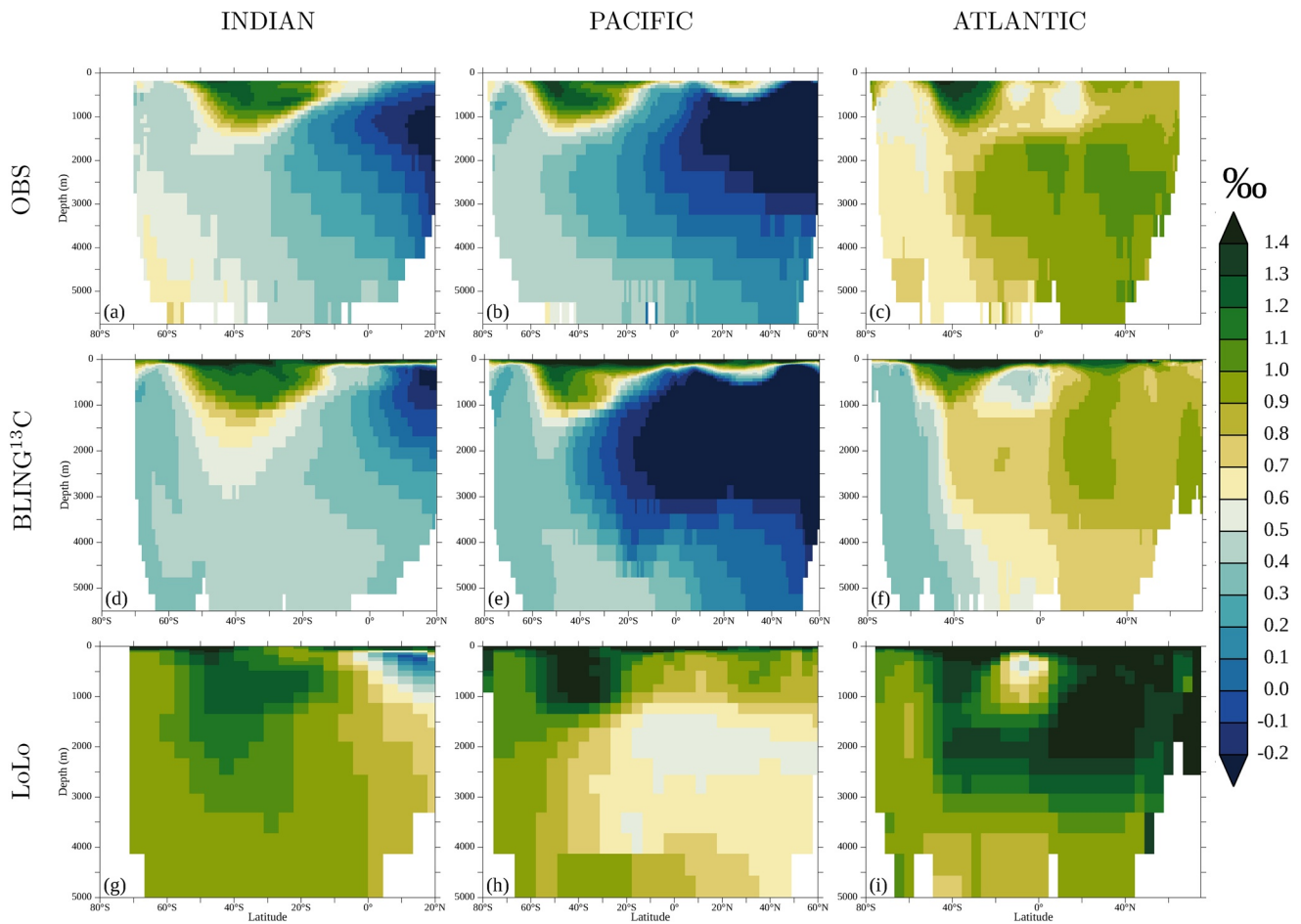
Figure 6. Zonally averaged sections of $\delta^{13}C_{DIC}$ (in ‰ units) across Indian (left), Pacific (middle), and Atlantic (right) ocean basins from ((a)–(c)) observations (OBS, Eide, Olsen, Ninnemann, & Johannessen, 2017), ((d)–(f)) MOM5-BLING^{13}C-*std* (BLING^{13}C), and ((g)–(i)) MOM3-OCMIP-LoLo (LoLo). Modeled sections are averaged between 1991 and 1998, enclosing the time period with maximum observational coverage on which the mapping of Eide, Olsen, Ninnemann, and Johannessen (2017) is based. As in Figure 3, MOM3-OCMIP-LoLo values have been corrected for the effect of riverine organic matter. BLING, Biogeochemistry with Light Iron Nutrients and Gas; OCMIP, Ocean Carbon Model Intercomparison Project.

vigorous vertical mixing in the model in this region, a common issue in upper and intermediate layers in GFDL-ESM2M and similar climate models (Sallée et al., 2013). In the North Atlantic the high $\delta^{13}C_{DIC}$ core of recently ventilated waters does not penetrate below 3,500 m in the model, in contrast to observations (Figures 6c and 6f), because the modeled Atlantic meridional overturning circulation is too shallow (Figure S3), a common bias in z*-coordinate models like ESM2M (Dunne, John, et al., 2012, their Figures 8a–8c). The modeled largest $\delta^{13}C_{DIC}$ departures from observations occur in regions where deep water is formed, that is, where physical controls on $\delta^{13}C_{DIC}$ are highly influenced by circulation and air-sea exchange. If the global model-data $\delta^{13}C_{DIC}$ mismatch was due to problems with biological parameterizations, the largest bias would be in the deep Pacific, where remineralization controls the $\delta^{13}C_{DIC}$ field (Broecker & Maier-Reimer, 1992). Next, we evaluate controls on $\delta^{13}C_{DIC}$ at the source of deep water masses.

3.2. Understanding ^{13}C at Depth

The deep ocean $\delta^{13}C_{DIC}$ field is shaped by the relative influences of air-sea CO_2 gas exchange, the global meridional overturning, and remineralization of ^{13}C-depleted exported organic matter. The former imprints a characteristic $\delta^{13}C_{DIC}$ signature on deep waters masses when these are formed at high latitudes. The meridional overturning rate impacts deep $\delta^{13}C_{DIC}$ in two ways. It determines the surface water residence time to which $\delta^{13}C_{DIC}$ yields a sensitivity, in contrast to Chlorofluorocarbons (CFCs) nor CO_2, given the long
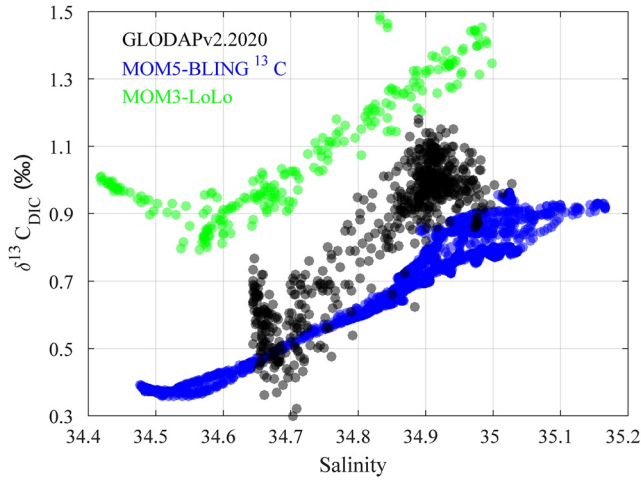
Figure 7. Distribution of $\delta^{13}C_{DIC}$ (in ‰ units) as a function salinity (unitless) for the deep Atlantic Ocean (between 75°S and 75°N below 2,000 m) in GLODAPv2.2020 observations (black), MOM5-BLING13C-*std* (blue), and MOM3-OCMIP-LoLo (green). Observational data is binned over 5° latitude bands that are 100 m thick and model output is zonally averaged. MOM3-OCMIP-LoLo has been corrected for the influence of riverine organic matter as in Figures 3c and 3d. BLING, Biogeochemistry with Light Iron Nutrients and Gas; DIC, dissolved inorganic carbon; OCMIP, Ocean Carbon Model Intercomparison Project.

$^{13}CO_2$ air-sea equilibration time (~10 years) and distributes the distinct $\delta^{13}C_{DIC}$ signature of source water masses across the deep ocean. These controls on $\delta^{13}C_{DIC}$ can be decomposed into physical ($\delta^{13}C_{as}$) and biological ($\Delta\delta^{13}C_{bio}$) components (Broecker & Maier-Reimer, 1992; Charles et al., 1993; Lynch-Stieglitz et al., 1995) as

$$\delta^{13}C_{DIC} = \delta^{13}C_{as} + \Delta\delta^{13}C_{bio} = \delta^{13}C_{as} - R_{13C:P}PO_4 + C_0, \quad (2)$$

where $R_{13C:P}$ is the ratio of $\delta^{13}C_{DIC}$ to PO_4, and C_0 is a constant chosen to yield a mean $\delta^{13}C_{as}$ of Pacific deep waters equal to zero (Broecker & Maier-Reimer, 1992). We defer to call $\delta^{13}C_{as}$ as preformed $\delta^{13}C_{DIC}$ because physical and biological controls are not fully separated in the latter tracer (Charles et al., 1993; Schmittner et al., 2013). We evaluate model biases in deep $\delta^{13}C_{DIC}$ controls using this decomposition.

3.2.1. Biology: $\Delta\delta^{13}C_{bio}$ from Abyssal PO_4 Versus $\delta^{13}C_{DIC}$

The biological contribution to $\delta^{13}C_{DIC}$ at depth can be estimated empirically from the slope of $\delta^{13}C_{DIC}$ versus PO_4 ($R_{13C:P}$) in the abyssal Pacific Ocean (below 2,000 m from 30°S to 30°N) as it is a basin with a single source of deep water input. In this basin, increases in PO_4 (ΔPO_4) caused by remineralizing organic matter decreases the $\delta^{13}C_{DIC}$ as a function of the $\delta^{13}C$ of organic matter ($\delta^{13}C_{org}$) and the carbon to phosphate ratio of organic matter ($C:P_{org}$) as follows (Broecker & Maier-Reimer, 1992)

$$R_{13C:P} = -\Delta\delta^{13}C_{bio} / \Delta PO_4 = -\delta^{13}C_{org} \times C:P_{org} / DIC_{mean}, \quad (3)$$

where DIC_{mean} is the mean DIC over the abyssal Pacific. In the GLODAPv2.2020 data set, the slope of the $\delta^{13}C_{DIC}$ versus PO_4 is -1.01 ± 0.02‰ (μmol kg^{-1})$^{-1}$ (Figure 9a) slightly different from the -1.1‰ (μmol kg^{-1})$^{-1}$ reported by Broecker and Maier-Reimer (1992) from a more limited data set. This shallowing of $R_{13C:P}$ between datasets is unlikely caused by the ^{13}C Suess effect as in the North Atlantic (Olsen & Ninnemann, 2010). Although the datasets are about 20 years apart, the penetration of CFCs (Fine et al., 2001;
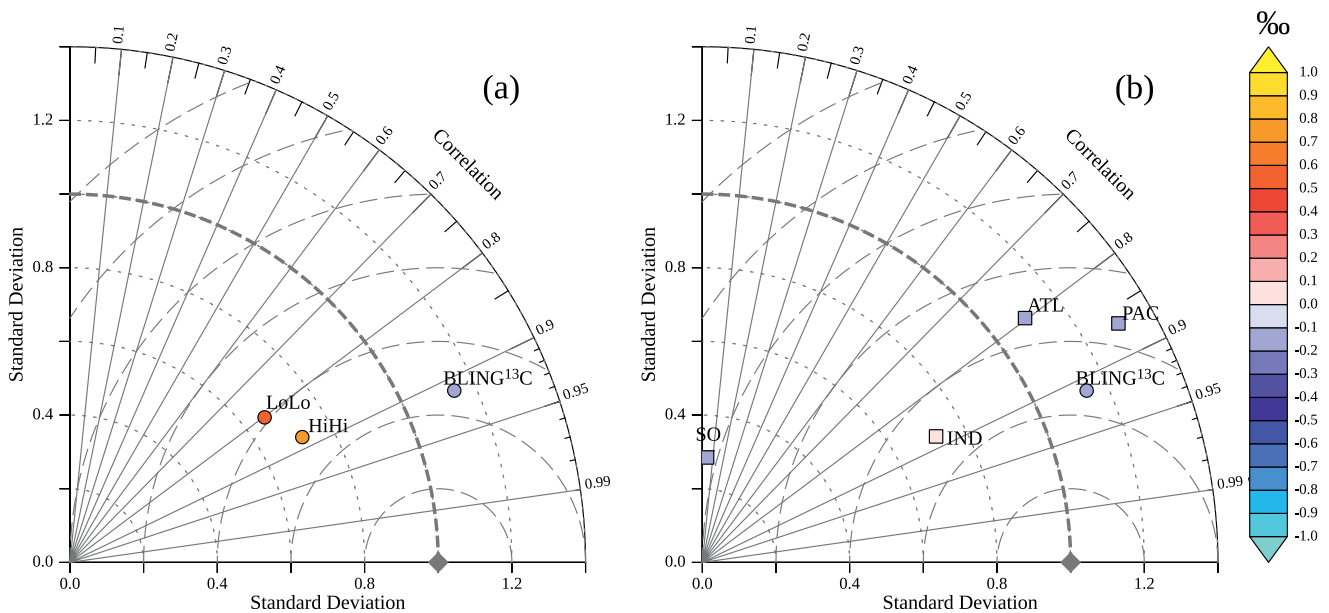
Figure 8. Same as Figure 4 but below 1,000 m for (a) global fields among GFDL models and (b) basin fields in MOM5-BLING13C-*std*. GFDL, Geophysical Fluid Dynamics Laboratory.
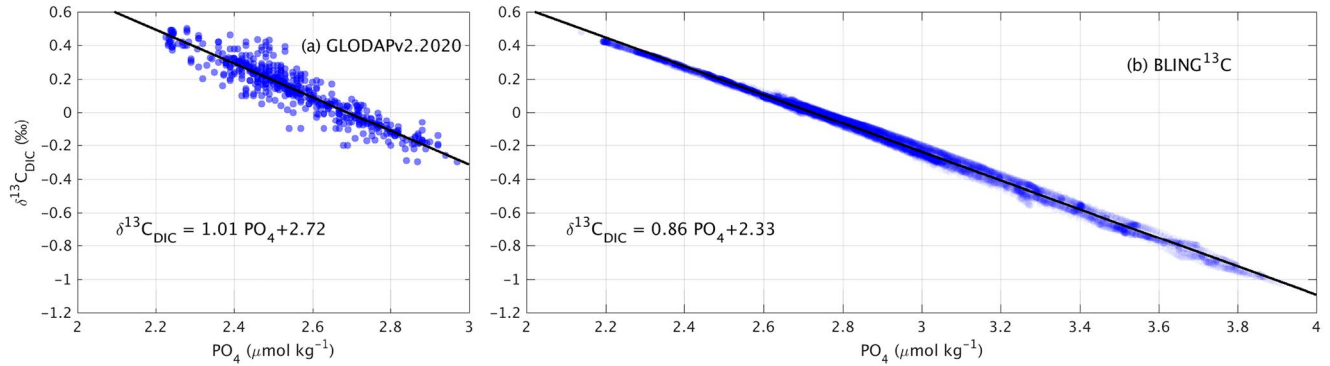
Figure 9. $\delta^{13}C_{DIC}$ as a function of PO_4 in (a) GLODAPv2.2020 observations and in (b) MOM5-BLING^{13}C-*std* model for the deep Pacific Ocean (defined between 30°S and 30°N and below 2,000 m). A linear polynomial is fit to point values to find the slope of $\delta^{13}C_{DIC}$ versus PO_4 ($R_{13C:P}$) and the intercept, which is the C_0 constant used to later compute $\delta^{13}C_{as}$. Note that the *x*-axis of MOM5-BLING^{13}C-*std* output has been extended to accommodate high PO_4 values so that observational and modeled grids are comparable. BLING, Biogeochemistry with Light Iron Nutrients and Gas; DIC, dissolved inorganic carbon.

Sonnerup et al., 2015) or changes in $\delta^{13}C_{DIC}$ (Ko et al., 2014) have not yet been detected in this region below 2,000 m. A $\Delta\delta^{13}C_{bio}/\Delta PO_4$ slope of $-1.01‰$ (μmol kg^{-1})$^{-1}$, assuming a C:P$_{org}$ of 117 (Anderson & Sarmiento, 1994), implies a mean $\delta^{13}C$ of remineralized organic matter of $-20.07‰$ (for DIC$_{mean}$ of 2,325 μmol kg^{-1}), in excellent agreement with the Goericke and Fry (1994) compilation for this latitude band ($-20.1 \pm 1.3‰$, see also Sonnerup et al., 1999, for a tabulation). However, the $\delta^{13}C$ versus PO_4 slope at depth has been established over hundreds of years, so $\delta^{13}C_{org}$ from Equation 3 reflects the preindustrial condition, which was approximately 1‰ enriched relative to today (Quay et al., 2003, 2017). Assigning instead a $\delta^{13}C_{org}$ of $-19‰$ yields a C:P$_{org}$ of 124 ± 10, not significantly different from the Anderson and Sarmiento (1994) value of 117 ± 14. It appears then that the deep $\delta^{13}C_{DIC}$ versus PO_4 slope in the Pacific Basin accurately reflects, within uncertainties, the $\delta^{13}C_{org}$ of the overlying sea surface.

Applying the same treatment to BLING^{13}C output in the same basin yields a $\delta^{13}C_{DIC}$ versus PO_4 slope of $-0.8563 \pm 6 \times 10^{-4}‰$ (μmol kg^{-1})$^{-1}$ (Figure 9b). In the model, C:P$_{org}$ is fixed at 106, and the mean DIC of this region is 2,387 μmol kg^{-1}, indicating a preindustrial $\delta^{13}C_{org}$ of $-19.28‰$, in excellent agreement with the preindustrial sea surface $\delta^{13}C_{org}$ in the model ($-19.23‰$, from 30°S to 30°N). If C:P$_{org}$ of 124 was used in BLING the $\delta^{13}C_{DIC}$ versus PO_4 slope in the abyssal Pacific would be $-1‰$ (μmol kg^{-1})$^{-1}$, as in the observations. BLING^{13}C's lower abyssal $\delta^{13}C_{DIC}$ versus PO_4 slope is caused by a low C:P$_{org}$ and not by a $\delta^{13}C_{org}$ that is too high. This model bias would lower the biological contribution to deep-sea $\delta^{13}C_{DIC}$ (computed as $R_{13C:P}$ PO_4) by about 0.3‰ considering the observed global mean PO_4 concentration (2.1 μmol kg^{-1} below 2,000 m after binning data into $1° \times 1° \times 500$ m cells). However, the model yields a higher mean PO_4 concentration (2.3 μmol kg^{-1}), which compensates for about half of this bias. This is because of an accumulation of PO_4 in the deep Pacific as a result of a slow meridional overturning as seen next.

3.2.2. Physics: $\delta^{13}C_{as}$ and Circulation's Impact on the Deep Sea $\delta^{13}C_{DIC}$

Once the $\delta^{13}C_{DIC}$ to PO_4 ratio ($R_{13C:P}$) is known, the influence of air-sea exchange and circulation, $\delta^{13}C_{as}$, is computed as the residual between total $\delta^{13}C_{DIC}$ and $\Delta\delta^{13}C_{bio}$ using Equation 2. $\delta^{13}C_{as}$ is only modified at the surface during air-sea CO_2 gas exchange, that is, it behaves as a quasi-conservative tracer once it leaves the mixed layer. Thus, $\delta^{13}C_{as}$ in the interior is driven by mixing and the $\delta^{13}C_{as}$ characteristics of source waters. Broecker and Maier-Reimer (1992) and Charles et al. (1993) showed that two water masses dominate the deep ocean $\delta^{13}C_{as}$: North Atlantic Deep Water (NADW) and Southern Ocean Deep Water (SODW; Figure 7). Sonnerup and Quay (2012) further showed that models with different relative proportions of NADW and SODW result in different deep sea $\delta^{13}C_{DIC}$. In this section, the mean deep ocean $\delta^{13}C_{as}$ will thus be approximated following this simple mixing model:

$$\delta^{13}C_{as} \sim \delta^{13}C_{as}^{MIX} = f^{SODW}\delta^{13}C_{as}^{SODW} + \left(1 - f^{SODW}\right)\delta^{13}C_{as}^{NADW}, \tag{4}$$
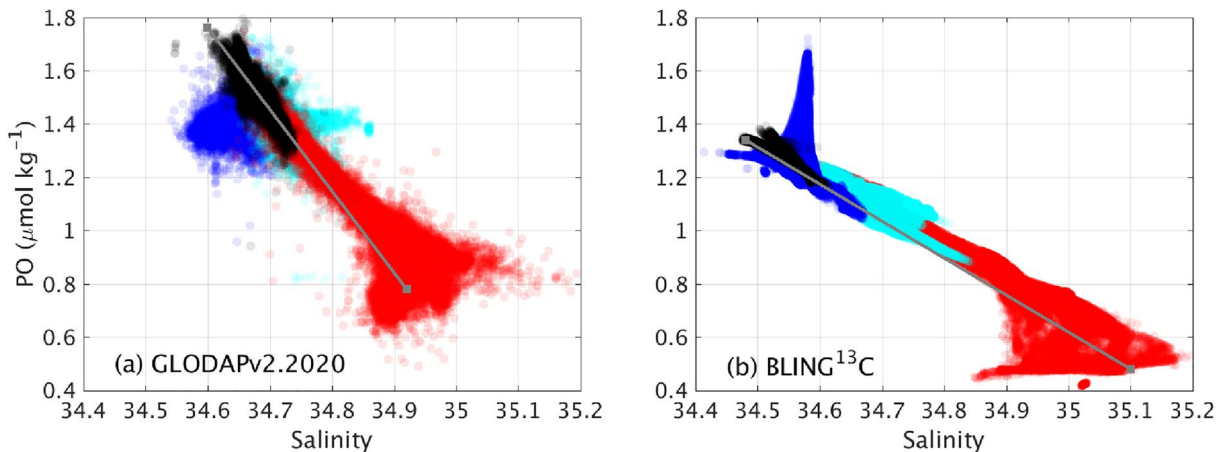
Figure 10. Subsurface (below 2,000 m) distribution of salinity (S) as a function of preformed phosphate (PO) for (a) GLODAPv2.2020 observations and (b) MOM5-BLING^{13}C-*std* model. Colors correspond to the Atlantic (red), Indian (cyan), Pacific (blue), and Southern Ocean (black). NADW and SODW S-PO endmember values are denoted with gray squares and the linear mixing between the two with a straight line. BLING, Biogeochemistry with Light Iron Nutrients and Gas; NADW, North Atlantic deep water; PO, preformed phosphate; SODW, Southern Ocean deep water.

where f^{SODW} is the fraction of SODW relative to NADW, and $\delta^{13}C_{as}^{NADW}$ and $\delta^{13}C_{as}^{SODW}$ the $\delta^{13}C_{as}$ endmember values of NADW and SODW, respectively. This fraction is obtained by solving a system of linear equations based on two independent mixing models, one for salinity (S) and one for preformed phosphate (PO), via a least squares fit.

SODW and NADW (depth > 2,000 m) masses are distinct endmembers in a S versus PO plot, where PO = PO$_4$-AOU × (P:O$_2$) (Broecker, 1974). AOU is the Apparent Oxygen Utilization and P:O$_2$ is the ratio of phosphate to oxygen used in the model or, when applied to observations, 170 (Anderson & Sarmiento, 1994). Low salinity and high PO waters define waters of Southern Ocean origin, and vice-versa in the North Atlantic. These are mixed by the ocean circulation approximately linearly to define the characteristics of IndoPacific deep waters (Figure 10a). MOM5-BLING^{13}C-*std*'s S-PO plot is closer to linear than in nature, and the PO to S slope is shallower (Figure 10b). The former is likely due to the absence of Southern Ocean Intermediate Water (SOIW, minimum salinity water mass) at these depths in the model. The latter is the result of a model's deep water salinity range too large, associated to a high (low) salinity bias in the North Atlantic (Southern Ocean). This bias is also found in a similar configuration of GFDL-MOM4 forced with prescribed COREv2-NYF forcing (Griffies et al., 2009, Section 12.2). As these authors point out, the origin of this salinity bias is due to errors in heat and water surface fluxes, ocean circulation biases, and/or unrealistic mixing. Finally, the high PO values observed at a constant salinity of about 34.59 occur in the model because of a slower abyssal ventilation in the deep Pacific, which causes complete O$_2$ utilization. The modeled water age is about 860 older than observed since the model mean ^{14}C of Pacific deep waters (north of 20°S and deeper than 2,000 m) for prebomb year 1955 is −324.6‰ while that observed is −221‰ (Sonnerup & Quay, 2012). When waters become oxygen depleted, PO$_4$ and O$_2$ cycles decouple both in nature and in BLING, which is configured so that it does not allow negative O$_2$ concentrations. In nature, such strong and deep anoxia does not occur in the Pacific so observed PO values do not surpass the SODW endmember's PO value.

A third circulation feature apparent in S-PO space is the model's stronger influence of SODW on IndoPacific deep waters relative to NADW. The relative contribution of source water masses can be quantified by a two-endmember mixing model, analogous to Equation 4, using S and PO (Broecker et al., 1998). In the observations, endmember values are revisited using the extended GLODAPv2.2020 data set. For the NADW, averages of data binned into 1° × 1° × 500 m regular cells are used for waters north of 55°N and south of 75°N of the deep ocean (below 2,000 m). For the SODW ones, S and PO are extrapolated to a potential temperature of $\theta = -1.8°C$ (Figure S4) to account for Ross Sea water formation (Broecker et al., 1998). Using the values specified in Table 2, IndoPacific deep waters (north of 40°S and below 2,000 m) are about two thirds composed by SODW ($f^{SODW} = 0.65$) and one third by NADW. For MOM5-BLING^{13}C-*std*, S and PO

Table 2
Endmember Values for Salinity (S, Unitless) and for Preformed Phosphate (PO, $\mu mol\ kg^{-1}$) Used to Compute the Relative Contribution of Southern Ocean Deep Water (SODW, f^{SODW}) and North Atlantic Deep Water (NADW, $1 - f^{SODW}$) for IndoPacific Deep Waters (Below 2,000 m and North of 40°S) Using a Least Squares Fit for Observations (GLODAPv2.2020 Data Set) and MOM5-BLING^{13}C-std

	S^{NADW}	S^{SODW}	PO^{NADW}	PO^{SODW}	S	PO	f^{SODW}
Observations	34.92	34.60	0.78	1.76	34.69	1.41	0.65
MOM5-BLING^{13}C-*std*	35.10	34.48	0.48	1.34	34.60	1.22	0.84

IndoPacific mean values are computed by previously binning data into $1° \times 1° \times 500$ m cells.

Abbreviations: BLING, Biogeochemistry with Light Iron Nutrients and Gas; NADW, North Atlantic deep water; PO, preformed phosphate; SODW, Southern Ocean deep water.

endmember values are defined as mixed layer-averaged values where deep convection occurs, diagnosed in the model as regions where the mixed layer depth exceeds 1,000 m, using the model's monthly climatology for the 1990s (Figure 11a). In the Southern Ocean, modeled S and PO endmembers are clearly defined (Figures 10b–10c, black crosses). In the North Atlantic, however, several endmembers exist (red crosses) and the mean value is taken (Table 2) over waters with salinity higher than 34.85 as waters with lower salinity values do not contribute to deep North Atlantic extrema (Figure 10b). The modeled IndoPacific deep waters are composed of 84% SODW and 16% NADW, indicating a too-large portion of waters formed in the Southern Ocean in the model than in nature.

Air-sea effects impact on the deep ocean through $\delta^{13}C_{as}$ endmember values

The effects of isotopic fractionation during air-sea CO_2 gas exchange in deep water formation regions propagate to the deep sea. At high latitudes air-sea CO_2 gas exchange enriches $\delta^{13}C_{as}$ while at low latitudes gas exchange depletes $\delta^{13}C_{as}$ (Figure 12) due to the temperature dependence of CO_2-DIC $\delta^{13}C$ equilibration (Zhang et al., 1995). However, $\delta^{13}C_{as}$ in surface waters of the subpolar North Atlantic where NADW forms is not significantly higher than $\delta^{13}C_{as}$ in subtropical and tropical latitudes. This observation is a result of two effects, first, surface waters in the subpolar North Atlantic were transported there from equatorial and tropical latitudes where air-sea CO_2 gas yields depleted $\delta^{13}C_{as}$ (Broecker & Maier-Reimer, 1992) and, second, there is insufficient time during the surface water transit at high latitudes to reset the $\delta^{13}C_{as}$ by gas exchange (i.e., air-sea $\delta^{13}C$ equilibration time is ~10 years). In contrast, SODW is formed from recently upwelled deep water within the Southern Ocean (Talley, 2013), which has an enriched $\delta^{13}C_{as}$ signature. This difference in deep water formation processes yields the distinct $\delta^{13}C_{as}$ signature for NADW and SODW waters masses.

The isotopic enrichment of SODW relative to NADW is evident in $\delta^{13}C_{as}$-PO plots for the deep ocean (depth > 2,000 m). The two source waters lie on opposite extrema and mix across basins in proportion with their relative contribution to deep waters (Figure 13a), f^{SODW}. To reveal the linear mixing trend between these endmembers the ^{13}C Suess effect needs to be subtracted, especially in the North Atlantic where this effect is the largest (see Figure 12 in Eide, Olsen, Ninnemann, & Eldevik, 2017). A preindustrial $\delta^{13}C_{as}$ is computed in observations using first Eide's MLRs to obtain preindustrial $\delta^{13}C_{DIC}$ (see Equation 2 of Eide, Olsen, Ninnemann, & Johannessen, 2017) and subtracting later the biological component $\Delta\delta^{13}C_{bio}$ (Equation 2). Resulting preindustrial $\delta^{13}C_{as}$ values for the North Atlantic (north of 20°N, purple dots with PO < 1.2 $\mu mol\ kg^{-1}$ in Figure 13a) align linearly with contemporary $\delta^{13}C_{as}$ values of the remaining basins in contrast to industrial $\delta^{13}C_{as}$ values, which show a steeper $\delta^{13}C_{as}$ to PO slope. This is likely associated with the ^{13}C Suess effect influence on the $\delta^{13}C_{DIC}$ to PO_4 slope in the North Atlantic since it drives a more prominent $\delta^{13}C_{DIC}$ decrease in waters of low PO_4 content relative to those with high PO_4 concentrations (Olsen & Ninnemann, 2010). The observed NADW $\delta^{13}C_{as}$ endmember value of −0.44‰ is obtained by averaging preindustrial $\delta^{13}C_{as}$ over waters with PO between 0.76 and 0.80 $\mu mol\ kg^{-1}$, centered around the NADW PO endmember value. In the Southern Ocean, preindustrial $\delta^{13}C_{as}$ (gray dots with PO > 1.3 $\mu mol\ kg^{-1}$ in Figure 13a) also align with global deep $\delta^{13}C_{as}$ values. For the SODW $\delta^{13}C_{as}$ endmember, preindustrial $\delta^{13}C_{as}$ are extrapolated to the SODW PO endmember of 1.76 $\mu mol\ kg^{-1}$ to obtain a value of 0.37‰ (Figure 13b). For comparison, Broecker and Maier-Reimer (1992) analysis of observations yielded isotopically lighter values for $\delta^{13}C_{as}$ NADW and SODW endmembers of −0.5‰ and 0.2‰ (their page 317), but these authors may not
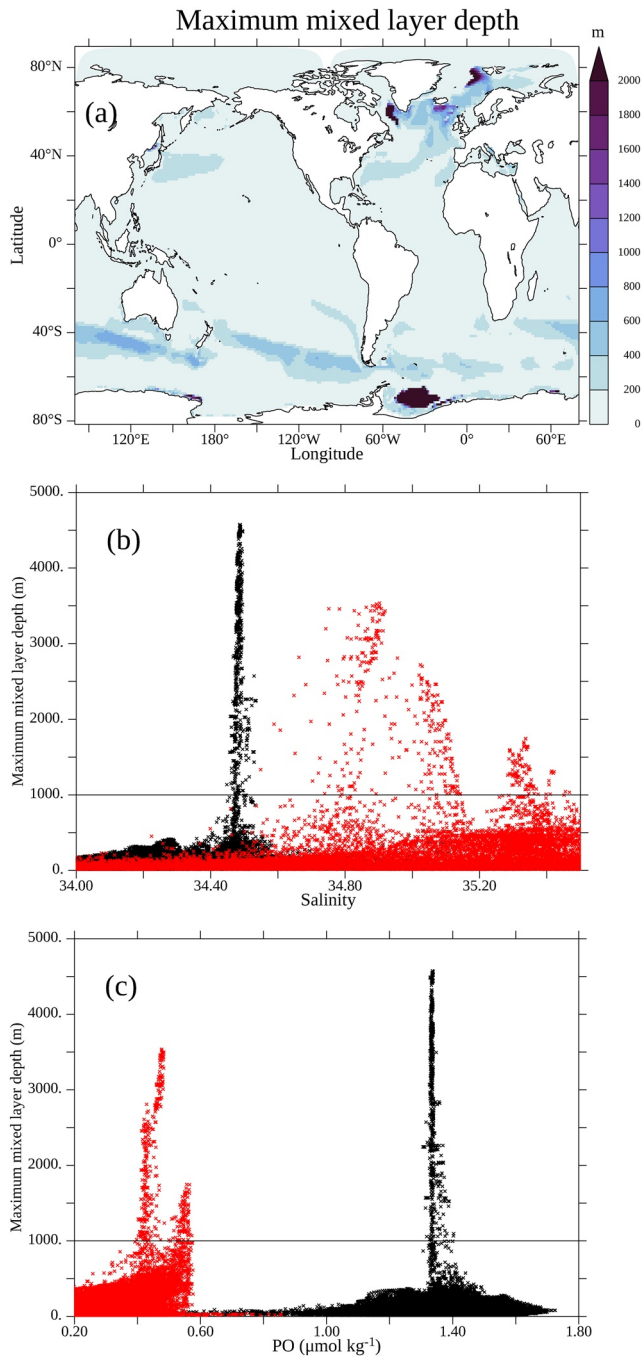
Figure 11. (a) Map of the modeled maximum mixed layer depth over a monthly climatology for the 1990–2002 period. Modeled mixed-layer averaged (b) salinity and (c) PO as a function of the climatological mixed layer depth in the Southern Ocean (south of 58°S, black) and the North Atlantic (north of 10°N, red). Endmember values correspond to mixed layers above 1,000 m, where deep convection occurs. PO, preformed phosphate.

have corrected for the ^{13}C Suess effect. The mixing model (Equation 4) then yields a $\delta^{13}C_{as}$ mean for Pacific deep waters of 0.08‰, close to that observed (−0.02 ± 0.08‰, Table 3).

Modeled deep $\delta^{13}C_{as}$ are isotopically lighter than observed (Figure 13c). This is because the upper bound of $\delta^{13}C_{as}$ corresponding to the Southern Ocean is too low, even when correcting for the ^{13}C Suess effect. Biases in the model's circulation affect the linearity of the mixing between source waters but also $\delta^{13}C_{as}$ endmember values given the long equilibration time of $^{13}CO_2$ with the atmosphere. The lack of Ross Sea water formation in the model (shown by shallow MLD in the Ross Sea, Figure 11a) and the missing pathway of Antarctic shelf-water export to the bottom contribute to a warm bias in the bottom potential temperature (between 1 and 2° in GFDL-ESM2M, i.e., Figure 1e in Heuzé et al., 2013) that probably decreases $\delta^{13}C_{as}$ due to the temperature dependence of fractionation during air-sea exchange. A slowed abyssal circulation rate and possible underestimations of the high latitude air-sea CO_2 gas exchange rate may also contribute to this bias in $\delta^{13}C_{as}$.

The two-endmember mixing model applied to observations is tested with model output to evaluate how model biases affect $\delta^{13}C_{DIC}$. Endmember values are diagnosed analogously to S-PO endmembers diagnosis -by looking at monthly climatological values averaged over the mixed layer in regions of deep convection- and correcting for the ^{13}C Suess effect (Figure 13d). Preindustrial NADW and SODW $\delta^{13}C_{as}$ endmembers are −0.38‰ and 0.07‰, which give a zero $\delta^{13}C_{as}$ mean of IndoPacific deep waters considering the value f^{SODW} = 0.84 estimated earlier. This value from the simplified mixing model (Equation 4) agrees well with the model direct solution (Table 3) showing that it is a good approximation to estimate deep-ocean $\delta^{13}C_{as}$. It is interestingly observed that in the North Atlantic, three endmembers exist for salinity (Figure 11b), corresponding to three deep convection sites, while only one exists for $\delta^{13}C_{as}$ (Figure 13d). This emphasizes the fact that the NADW $\delta^{13}C_{as}$ endmember is less sensitive to model biases in the ocean circulation than the SODW $\delta^{13}C_{as}$ endmember because it is largely influenced by air-sea CO_2 gas exchange at low and mid latitudes.

3.3. Ocean $\delta^{13}C_{DIC}$'s Dependence on the CO_2 Gas Exchange Rate

We tested the sensitivity of deep-sea $\delta^{13}C_{DIC}$ to the air-sea CO_2 gas exchange rate by increasing the air-sea gas coefficient about 34%, from 0.251 (OMIP-CMIP6 protocol) to 0.337 (OCMIP2 protocol). The most remarkable change in *fast-gas-exchange* compared to *standard* is the decrease of ∼0.2‰ in surface $\delta^{13}C_{DIC}$ at low and mid latitudes accompanied by a ∼0.2‰ increase at southern hemisphere high latitudes and a increase of ∼0.12‰ in the North Atlantic (Figures 14a and 14b). These changes are due to the larger influence of the temperature dependence gas-exchange fractionation with the atmosphere. The surface $\delta^{13}C_{DIC}$ pattern in the *standard* simulation shows better agreement with observations compared to the *fast-gas-exchange* one with a higher correlation coefficient, smaller RMSE, and a standard deviation closer to the observed one (Figures 4 and 14c, Table 1). Especially relevant is the decrease in the general bias of surface $\delta^{13}C_{DIC}$ in the Southern Ocean as one of the two regions of deep water mass formation.
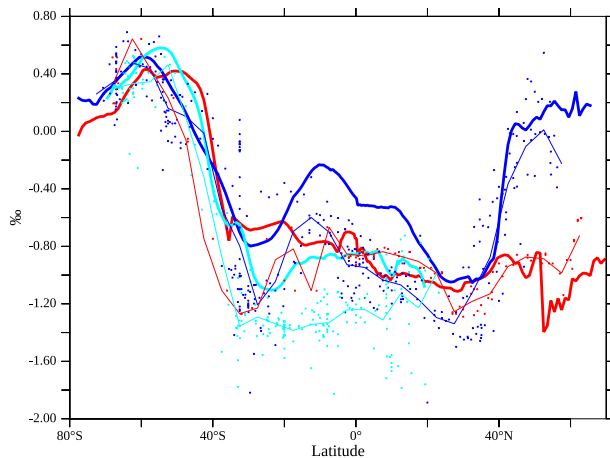
Figure 12. As in Figure 3b but for surface $\delta^{13}C_{as}$ computed using Equation 2. Values of $R_{13C:P}$ and C_0 are obtained from the linear regressions in Figure 9.

The increase in the air-sea CO_2 gas exchange rate decreases the vertical $\delta^{13}C_{DIC}$ gradient (Figures 15a–15c): not only does *fast-gas-exchange* decrease the low latitude surface $\delta^{13}C_{DIC}$, it also increases the deep ocean $\delta^{13}C_{DIC}$ because it increases $\delta^{13}C_{as}$ of the deep water source waters. Indeed, the modern $\delta^{13}C_{DIC}$'s mean of deep waters (below 2 km) is 0.15‰ higher in the *fast-gas-exchange* simulation relative to *standard* (0.43‰ vs. 0.28‰, see also Table 1), as it is the C_0 value of $\delta^{13}C_{as}$ for deep Pacific waters (2.47‰ vs. 2.32‰). When centered at $C_0 = 2.47$, the range between NADW and SODW endmember values increases in the *fast-gas-exchange* simulation relative to *standard* centered at $C_0 = 2.32$ (Table 3). The value of $\delta^{13}C_{as}^{NADW}$ becomes isotopically lighter, amplifying the memory $\delta^{13}C_{as}$ has from low and mid latitudes in the North Atlantic basin, while that of $\delta^{13}C_{as}^{SODW}$ becomes isotopically heavier. The increase in $\delta^{13}C_{as}^{SODW}$ drives ultimately the increase in the $\delta^{13}C_{DIC}$ mean of deep waters given the larger contribution of SODW relative to NADW. This is reflected in higher $\delta^{13}C_{DIC}$ values over the water column in the Southern Ocean (see Figures 15a–15c vs. 6d–6f) resulting is a slightly lower general bias and a higher correlation coefficient ($\sim$0.15) in this basin for the *fast-gas-exchange* simulation (Figures 15d vs. 8).

The meridional trend in surface $\delta^{13}C_{DIC}$ is much improved when using an air-sea CO_2 gas coefficient of 0.251, as recommended with COREv2 forcing in the newest generation of climate models within the OMIP-CMIP6 project (Orr et al., 2017). The reduction from 0.337 (OCMIP2 protocol, Najjar & Orr 1998), also results in a decrease of the $\delta^{13}C_{DIC}$ of the deep ocean. The fact that we matched the observed deep ocean $\delta^{13}C_{DIC}$ using a gas exchange rate of 0.337 (*fast-gas-exchange*, see Table 1) is likely due to compensating model biases in the ocean circulation, which influence the relative contribution of water masses but also the $\delta^{13}C_{as}$ endmember values.

4. Summary

We have constructed a model for oceanic ^{13}C that is a major improvement over prior GFDL-implementations (Sonnerup & Quay, 2012) because the abyssal circulation is more realistic, gas exchange and momentum fluxes are forced by the same wind fields, and because the biological pump is not prescribed, and it includes iron and light, features that make the MOM5-BLING^{13}C configuration suitable for longer term climate studies. MOM5-BLING^{13}C captured well inter-basin and meridional $\delta^{13}C_{DIC}$ variability and a substantial decrease in surface $\delta^{13}C_{DIC}$ south of 55°S that was missing in previous GFDL modeling efforts. However, some model biases remain, especially in the Atlantic and Southern Oceans. We used a Redfield-based tracer technique, built upon Broecker and Maier-Reimer (1992) and Charles et al. (1993), to decompose deep $\delta^{13}C_{DIC}$ into biological and physical components. Applying this technique to both GLODAPv2.2020 data and MOM5-BLING^{13}C output we found:

1. The $\delta^{13}C_{DIC}$ to PO_4 slope ($R_{13C:P}$) in the GLODAPv2.2020 deep Pacific data set is -1.01 ± 0.02‰ $(\mu mol\ kg^{-1})^{-1}$, rather than the canonical slope of -1.1‰ $(\mu mol\ kg^{-1})^{-1}$ determined from prior, smaller datasets (Broecker & Maier-Reimer, 1992). In MOM5-BLING^{13}C, the $R_{13C:P}$ of $0.8563 \pm 6 \times 10^{-4}$‰ $(\mu mol\ kg^{-1})^{-1}$ is lower than observed due to the lower C:P_{org} ratio of 106 used in the model and not to inaccuracies in the $\delta^{13}C$ of organic matter.
2. The Meridional Overturning Circulation (MOC) rate affects deep-ocean $\delta^{13}C_{as}$ in two ways, primarily via the north versus south proportionality of deep water masses, but also by controlling the preindustrial $\delta^{13}C_{as}$ endmember values, especially for Southern Ocean deep water. The latter is because the overturning rate influences the residence time of surface waters in regions of deep convection.
3. The ocean mean $\delta^{13}C_{DIC}$ is sensitive to the air-sea CO_2 gas exchange rate. Updating the CO_2 gas exchange coefficient from 0.337 (OCMIP2 protocol) to 0.251 (OMIP-CMIP6 protocol) significantly improved the sea surface $\delta^{13}C_{DIC}$, yielded more realistic meridional trends and reduced its bias and the root mean
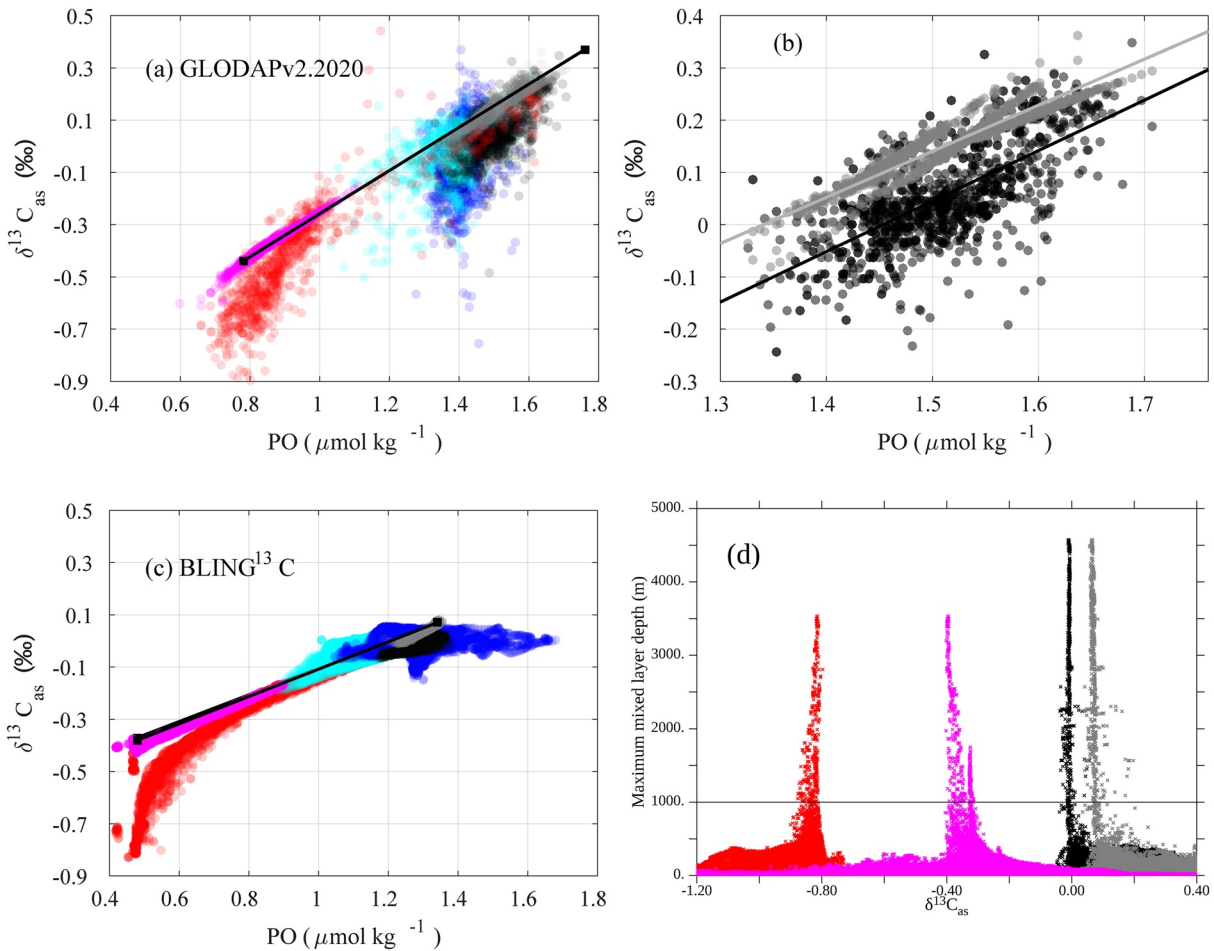
Figure 13. (a) As in Figure 10 but for deep ocean $\delta^{13}C_{as}$ as a function of PO for GLODAPv2.2020 observations. Purple and gray circles are preindustrial $\delta^{13}C_{as}$ values in the North Atlantic (north of 20°N) and the Southern Ocean (south of 58°S), respectively. NADW and SODW PO-$\delta^{13}C_{as}$ endmember values are denoted with black squares and the linear mixing between the two with a straight line. (b) Extrapolation of observed $\delta^{13}C_{as}$ to the SODW PO endmember value of 1.76 $\mu mol\ kg^{-1}$ for the deep Southern Ocean (south of 58°S and below 2,000 m) of modern GLODAPv2.2020 data (black dots) and with the ^{13}C Suess effect removed (gray dots). Linear regression between variables are shown with straight lines. (c) As in (a) but for MOM5-BLING^{13}C-*std* model output. (d) As in Figures 11b and 11c but for modeled $\delta^{13}C_{as}$ with preindustrial values in the North Atlantic and the Southern Ocean in purple and gray, respectively. BLING, Biogeochemistry with Light Iron Nutrients and Gas; NADW, North Atlantic deep water; PO, preformed phosphate; SODW, Southern Ocean deep water.

Table 3
Endmember Values of $\delta^{13}C_{as}$ for NADW and SODW Used to Compute the $\delta^{13}C_{as}$ Value of IndoPacific Deep Waters (Defined as in Table 2) Applying the Mixing model ($\delta^{13}C_{as}^{MIX}$)

	$\delta^{13}C_{as}^{NADW}$	$\delta^{13}C_{as}^{SODW}$	$\delta^{13}C_{as}^{MIX}$	$\delta^{13}C_{as}$
Observations	−0.44	0.37	0.08	−0.02 ± 0.08
MOM5-BLING^{13}C-*std*	−0.38	0.07	0	0
MOM5-BLING^{13}C-*fast*	−0.42	0.12	0.03	0

This latter value is compared to the observed and modeled $\delta^{13}C_{as}$ averages over the deep IndoPacific region (last column). Observational $\delta^{13}C_{as}$ mean and standard deviation are computed by previously binning data as in Table 2 and modeled means for the standard (*std*) and fast-gas-exchange (*fast*) simulations are volume-weighted.
Abbreviations: BLING, Biogeochemistry with Light Iron Nutrients and Gas; NADW, North Atlantic deep water; SODW, Southern Ocean deep water.
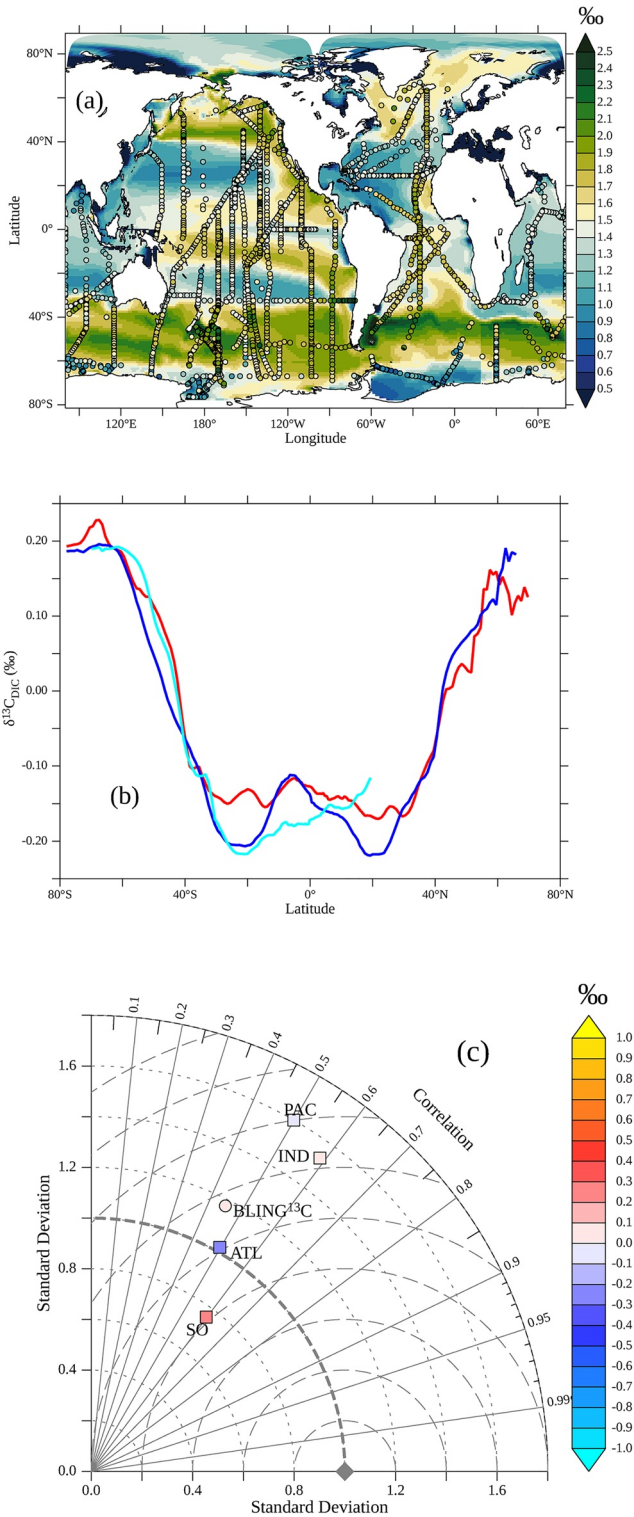
Figure 14. (a) Surface $\delta^{13}C_{DIC}$ field for the *fast-gas-exchange* simulation as in Figure 3a. (b) Difference between the *fast-gas-exchange* and the *standard* simulations of zonally averaged surface $\delta^{13}C_{DIC}$. Basins are color coded as in Figure 3b. (c) As in Figure 4 but for the *fast-gas-exchange* simulation. DIC, dissolved inorganic carbon.

square error. The changes in high latitude water mass formation regions translate into a lower deep-sea $\delta^{13}C_{DIC}$.

Our understanding of the mechanisms that shape $\delta^{13}C_{DIC}$ using ocean models has much advanced since first models appeared, yet still faces significant challenges. At the local scale, model-data mismatches in surface $\delta^{13}C_{DIC}$ can be large. In the Atlantic these may be due to riverine ^{13}C inputs. In the Southern Ocean, studies indicate that $\delta^{13}C$ of organic matter exported to depth may be heavier than that observed at the surface (Trull & Armand, 2001) and that parameterized in our model. Finally, ocean circulation biases relevant for ^{13}C remain, largely impacting the Southern Ocean and Atlantic Ocean. Models with z*-coordinates simulate a too shallow Atlantic MOC (AMOC), weighting the deep ocean water composition too heavily toward Southern Ocean deep waters. While isopycnal coordinate models improve the depth of the AMOC, unresolved Nordic Seas overflows still contribute to this bias (Adcroft et al., 2019). Because deep water formation on Arctic and Antarctic shelves is usually not resolved in ocean models, resulting in a lack of Ross Sea deep water formation in our model, it may partially explain the slower abyssal overturning than in nature. Improved mixing parameterizations and finer model resolution should improve the MOC, yielding improved deep ocean $\delta^{13}C_{DIC}$. Increasing ocean resolution comes, however, at a computational cost that is critical with ^{13}C-cycling given the long equilibration time of $\delta^{13}C_{DIC}$ (longer than 5,000 years). In this regard, the two-endmember mixing model presented here can be applied to estimate the mean deep $\delta^{13}C_{DIC}$ state, combining Equations 2–4, without awaiting for a full deep ocean steady state for $\delta^{13}C_{as}$.

In spite of biases above-mentioned, model-data fidelity has improved significantly over prior GFDL-based models. Our companion manuscript focuses on the anthropogenic ^{13}C response of this model, and applications toward estimating the global mean and preindustrial air-sea $\delta^{13}C$ disequilibrium. MOM5-BLING^{13}C is a logical step toward including ^{13}C in fully coupled atmosphere-ocean-ice GFDL climate models with the aim to evaluate natural and anthropogenic carbon fluxes between Earth's compartments. Although this model configuration was initially constructed to study the anthropogenic ^{13}C response, this model has promising applications toward longer time scales. For example, BLING^{13}C includes controls on the biological C-pump thought to be important in the Glacial ocean: light and iron limitation, and controls on ^{13}C of organic matter formation, and thus on ocean $\delta^{13}C_{DIC}$ and its vertical gradient, that depend on pCO_2.

Appendix A: BLING^{13}C Formulation

A1. ^{13}C Air-Sea Exchange

Isotopic fractionation during air-sea gas exchange for ^{13}C in Schmittner et al. (2013) follows Zhang et al. (1995), namely

$$F_{13_C}^{as} = k\alpha_k\alpha_{\text{aq}\leftarrow g}\left(R_{\text{atm}}CO_2^*\big|_{\text{sat}} - \frac{R_{DIC}}{\alpha_{\text{DIC}\leftarrow g}}CO_2^*\right), \quad (A1)$$

where k is the piston velocity (in cm hr^{-1}), R_{atm} the atmospheric ratio of $p^{13}CO_2$ to pCO_2 (dimensionless), and $CO_2^*\big|_{\text{sat}}$ the saturation concen-
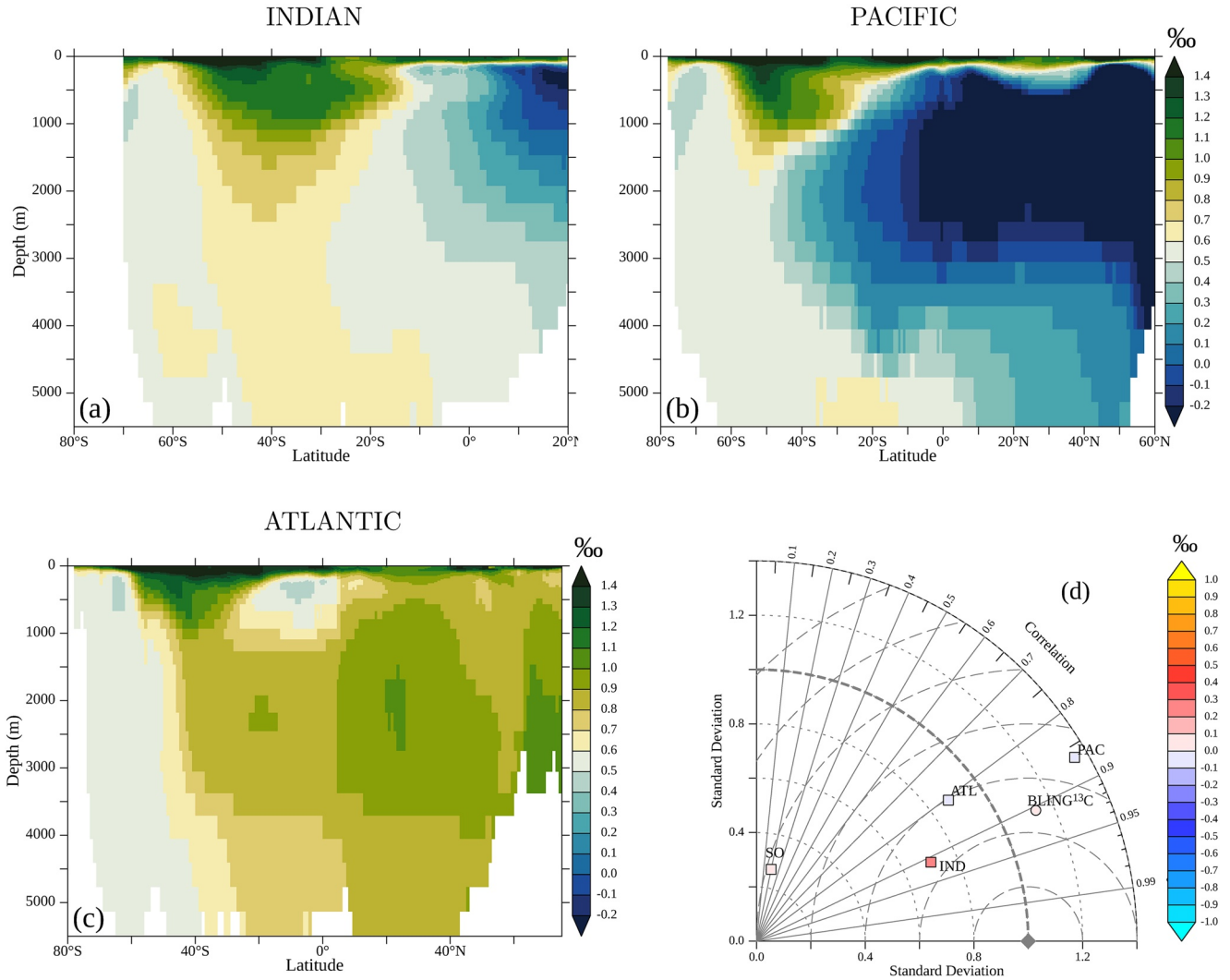
Figure 15. ((a)–(c)) Meridional sections of $\delta^{13}C_{DIC}$ as in Figures 6d–6f but for the *fast-gas-exchange* simulation. (d) Taylor diagram of subsurface $\delta^{13}C_{DIC}$ as in Figure 8b for the *fast-gas-exchange* simulation. DIC, dissolved inorganic carbon.

tration in equilibrium with the atmosphere (in mol m^{-3}). The piston velocity depends on a the air-sea gas coefficient factor k_0 (in $(cm\ hr^{-1})/(m\ s^{-1})^2$), the sea ice cover s (dimensionless), the wind speed at 10 m above sea level u (in m s^{-1}), and the Schmidt number Sc (dimensionless) according to

$$k = k_0(1-s)u^2\sqrt{660/Sc}.\qquad(A2)$$

Kinetic fractionation during air-sea exchange α_k is held constant at $\alpha_k = 0.99915$ ($\epsilon_k = -0.85\text{‰}$), which is an average value of ϵ_k measurements at 5°C and 21°C (Zhang et al., 1995). The isotopic fractionation from gas to dissolved gas $\alpha_{aq\leftarrow g}$ is defined as $(^{13}C/^{12}C)_{aq}/(^{13}C/^{12}C)_g$ and neglects the small temperature dependence of (Zhang et al., 1995). Instead, $\alpha_{aq\leftarrow g} = 0.99876$ ($\epsilon_{aq\leftarrow g} = -1.24\text{‰}$) is a constant that corresponds to the $\alpha_{aq\leftarrow g}$ value at 15°C as in Schmittner et al. (2013). Finally, the fractionation from dissolved gas to DIC $\alpha_{DIC\leftarrow g}$, being the ratio $(^{13}C/^{12}C)_{DIC}/(^{13}C/^{12}C)_g$, does not consider the minor dependence on the carbonate ion and is only a function of temperature following $\alpha_{DIC\leftarrow g} = 1.01051 - 1.05 \times 10^{-4}\ T$ (Zhang et al., 1995).

A2. ¹³C Organic Matter Fractionation

Isotopic fractionation of ^{13}C during photosynthetic production of organic matter ($\alpha_{OC\leftarrow DIC}$) follows Schmittner et al. (2013), namely

$$F_{13_C}^{prod} = \frac{\alpha_{aq \leftarrow g}}{\alpha_{DIC \leftarrow g}} \alpha_{POC \leftarrow aq} R_{DIC} C : P F_P^{prod}. \tag{A3}$$

Values for $\alpha_{aq \leftarrow g}$ and $\alpha_{DIC \leftarrow g}$ are explained above. The ratio of these two fractionation factors is the fractionation from DIC to aqueous CO_2. Fractionation during biological carbon uptake, depends on the CO_2 concentration according to $\alpha_{POC \leftarrow aq} = -0.017 \log\left(CO_2^*\right) + 1.0034$ (Popp et al., 1989), where CO_2^* is aqueous carbon dioxide plus carbonic acid. These fractionations are applied to the total production in terms of phosphate F_P^{prod} converted into carbon using the elemental Redfield C:P ratio (106).

A3. Production of $Ca^{13}CO_3$

The production of calcium carbonate includes an isotopic enrichment factor $\epsilon_{Ca \leftarrow DIC}$ of 1‰ (Bonneau et al., 1980) as

$$F_{Ca^{13}CO_3}^{prod} = \alpha_{ca \leftarrow DIC} R_{DIC} F_{CaCO_3}^{prod}, \tag{A4}$$

where $\alpha_{Ca} \leftarrow DIC = (\epsilon_{Ca} \leftarrow DIC/1,000) + 1$. This fractionation is applied to the production of $CaCO_3$, $F_{CaCO_3}^{prod}$.

Appendix B: $\delta^{13}C$ of DIC Definition in Models

The conventional definition of $\delta^{13}C$ of DIC is given by

$$\delta C_{DIC}^{13} \equiv \left(\frac{R_{DIC}}{R_{PDB}} - 1\right) \times 1000, \tag{B1}$$

being

$$R_{DIC} \equiv \left(\frac{DI^{13}C}{DI^{12}C}\right), \tag{B2}$$

and R_{PBD} the Pee Dee Belemnite standard $^{13}C/^{12}C$ ratio. This definition comes from the observational community given that the ^{13}C content in samples is not directly measurable and the $^{13}C/^{12}C$ ratio is measured instead. Ocean biogeochemical models, however, usually solve for DIC instead of $DI^{12}C$. Considering that 98.9% of DIC is composed of $DI^{12}C$, these models approximate R_{DIC} as

$$R_{DIC} \simeq \frac{DI^{13}C}{DIC} \tag{B3}$$

(e.g., Orr et al., 2017; Schmittner et al., 2013). Given that the $DI^{13}C$ concentration is explicitly resolved in modeling, confusion may then arise in models that solve for DIC on whether $\delta^{13}C_{DIC}$ should be computed using the R_{DIC} definition of (B3) or that of (B2) considering $DI^{12}C = DIC - DI^{13}C$. This note demonstrates that the R_{DIC} to be used to compute modeled $\delta^{13}C_{DIC}$ needs to be consistent with that used in the ^{13}C-cycling model formulation. To this end, we consider an extremely idealized scenario where the oceanic mixed layer exchanges CO_2 with an atmosphere that is permanently depleted of carbon. Neglecting biological processes, the C-system governing equations according to Zhang et al. (1995), are

$$\frac{dDI^{12}C}{dt} = -k^{12}CO_2^{aq}, \tag{B4}$$

$$\frac{dDI^{13}C}{dt} = -k\alpha^{12}CO_2^{aq}R_{DIC}, \tag{B5}$$

where k is the piston velocity and α a fractionation factor that combines kinetic, solubility, and carbon speciation fractionations that is independent of surface aqueous CO_2 concentration of carbon-12 ($^{12}CO_2^{aq}$). Assuming that 1% of $DI^{12}C$ is $^{12}CO_2^{aq}$ (in the ocean it ranges between 0.35% and 1.5%) and using the R_{DIC} definition of (B2), the system of equations above can be combined to a single equation,

$$\frac{dR_{DIC}}{dt} = k(1-\alpha)0.01R_{DIC},\qquad(B6)$$

which has the following direct solution

$$R_{DIC}(t) = R_0 \exp\left\{k(1-\alpha)0.01t\right\},\qquad(B7)$$

being R_0 the R_{DIC} ratio at initial time.

If the approximation $DI^{12}C \simeq DIC$ is next made, the C-system equations to solve is

$$\frac{dDIC}{dt} = -kCO_2^{aq},\qquad(B8)$$

$$\frac{dDI^{13}C}{dt} = -k\alpha CO_2^{aq}R_{DIC},\qquad(B9)$$

Assuming that $CO_2^{aq} = 0.01DIC$, as before and using the R_{DIC} definition of (B2), the combination of (B8) and (B9) gives now

$$\frac{dR_{DIC}}{dt} = k0.01R_{DIC}(1 + R_{DIC})\left[1 - \alpha(1 + R_{DIC})\right],\qquad(B10)$$

to which (B7) is not a solution. For an approximation to be valid, the approximated system should behave in the same way as the original system. To this end, the R_{DIC} definition of (B3) should be used with (B8)–(B9) so that its solution is (B7), the same as the (B4)–(B5) system.

Finally, we illustrate that using a $\delta^{13}C$ definition that is inconsistent with the ^{13}C-cycling formulation can result in significant errors. It is first noted that the R_{DIC} definition in (B2), hereinafter R_1, is related to that in (B3), hereinafter R_2, through $R_1 = R_2/(1 - R_2)$. Considering the case where $R_2 = R_{PDB}$ for example, then $\delta^{13}C_{DIC}(R_{DIC} = R_2) = 0$, while $\delta^{13}C_{DIC}(R_{DIC} = R_1) = 11.36‰$. The latter value would be the associated error when using the C-system governing equations of B8–B9 with the R_{DIC} definition of (B2) to compute $\delta^{13}C_{DIC}$. This is a non-negligible difference given that it is of the same order of magnitude than the $\delta^{13}C$ range in the ocean.

Appendix C: MOM5-BLING^{13}C Model Evaluation

A physical steady state was reached with a globally volume-weighted average temperature and salinity of 4.08°C and 34.72, respectively (Figure C1a). This is in agreement with the GFDL-MOM4 ice-ocean coupled model forced with the same atmospheric data set (COREv2-NYF) described in Griffies et al. (2009). The Atlantic Meridional overturning circulation stabilized between 18 and 19 Sv at 45°N (Figure C1a, black line), which agrees reasonably well with observed estimates at mid latitudes, about 13–15.5 ± 2 Sv (see Section 4.1.1 in Buckley & Marshall, 2016). Regarding biogeochemical tracers, total inorganic phosphate PO_4 was invariant during the simulations, as no external phosphate sources/sinks were considered, with a volume-weighted mean of 2.3 μmol kg^{-1}. This global mean compares well with the observed depth-weighted mean of 2.1 ± 0.4 μmol kg^{-1} computed for an averaged macronutrient as $1/2(PO_4 + NO_3/16)$ using World Ocean Atlas 2018. Observed macronutrients are averaged using the P:N Redfield ratio 1:16 to compare with the modeled PO_4 tracer since the latter represents a generic macronutrient as nitrogen fixation and denitrification processes are not resolved in BLING. The global ocean oxygen inventory reached an equilibrium with a concentration of 210 Pmol (Figure C1b), about 17 Pmol lower than the observed inventory (see Table 1
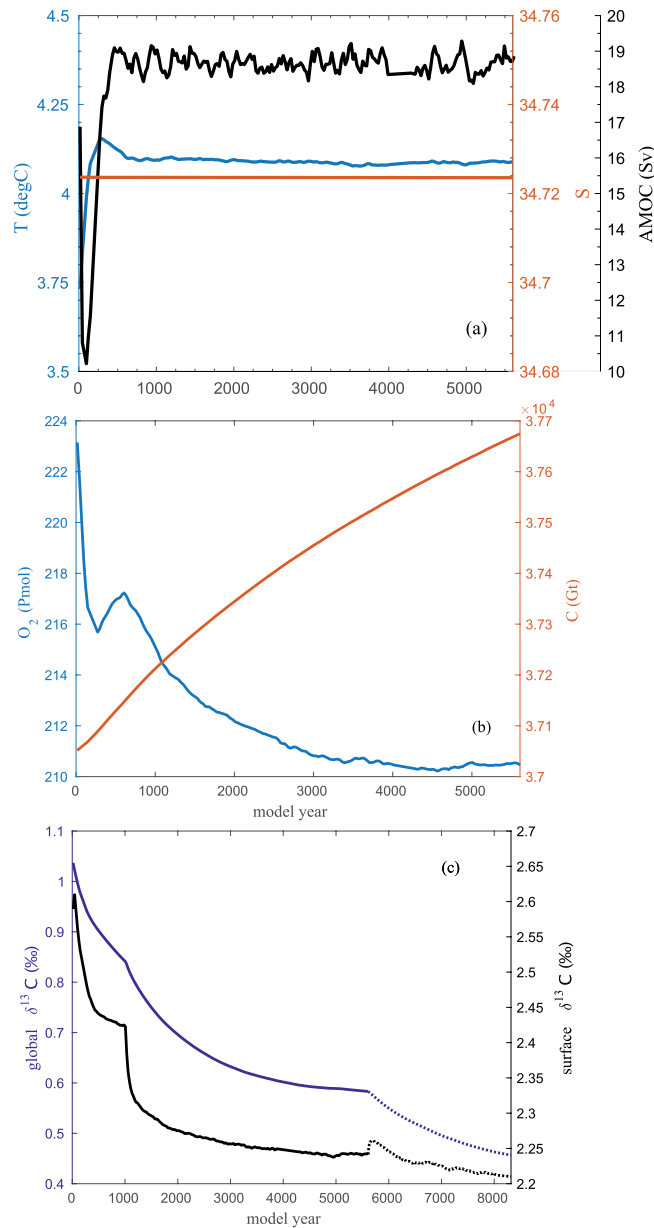
Figure C1. Time evolution over the *fast-gas-exchange* simulation spin up phase of temperature (blue), salinity (orange) and the Atlantic Meridional Overturning Circulation (AMOC, black) in (a); oxygen (blue) and carbon (orange) inventories in (b); and global (blue) and surface (0–10 m, black) $\delta^{13}C_{DIC}$ mean in (c). In (c), averages for the spin up phase of the *standard* simulation are also included in dotted lines. All values are volume-weighted averages.

in Schmidtko et al., 2017). The total carbon inventory (DIC + DOP × C:P) was 37,700 Gt C at the end of the spin up (Figure C1b). Although this concentration was close to the preindustrial oceanic carbon pool estimated at about 38,000 Gt C (Sarmiento & Gruber, 2006) it was increasing at a rate of 0.09 Gt C yr^{-1}. The fact that the carbon cycle was not in equilibrium is because of the long timescale of calcite burial (about 10,000 years), which in a full steady state system would be balanced by air-sea and riverine carbon fluxes. Indeed, the modeled carbon drift was the residual between a riverine input of 0.45 Gt C yr^{-1} minus a net CO_2 air-sea evasion of 0.17 Gt C yr^{-1} and a carbon burial flux of 0.2 Gt C yr^{-1}. This carbon drift had a small effect in ^{13}C since global and surface ocean $\delta^{13}C_{DIC}$ drifted about -5×10^{-3}‰ and -2×10^{-4}‰, respectively, over the last 500 years of the spin up of the *fast-gas-exchange* simulation (Figure C1c, solid line). For the *standard* simulation, the $\delta^{13}C_{DIC}$ drift was twice that of the *fast-gas-exchange* one (-0.01‰) over the last

Table C1
Global ocean preindustrial carbon fluxes after the 6,000 years long spin up for reference

	MOM5-BLING[13]C-*fast*	Observations
Natural air-sea CO_2 flux	0.17	0.2–0.4[1]
Carbon burial flux	0.2	0.1[1]
Primary productivity	63.52	44–57[2]
Particle export rate	10.57	(9.6 ± 3.6)[3]

Abbreviation: BLING, Biogeochemistry with Light Iron Nutrients and Gas.
[1]Sarmiento and Sundquist (1992). [2]Carr et al. (2006). [3]Dunne et al. (2007).

500 years as the spin up phase was ran for about half the period of the former (Figure C1c, dotted line). The surface $\delta^{13}C_{DIC}$ drift was, however, much smaller than the global one with a value of -6×10^{-3}‰.

Finally, relevant rates of the preindustrial carbon cycle (in units of Gt yr^{-1}) at the end of the ~6,000 yr long spin up phase of the *fast-gas-exchange* simulation are stated in Table C1 for reference. Modeled primary productivity is integrated over the upper 100 m layer and the modeled particle export is computed at 100 m depth as in Galbraith et al. (2010, 2015).

Data Availability Statement

Surface $\delta^{13}C_{DIC}$ data are available at BCODMO (http://www.bco-dmo.org/data). Deep ocean hydrographic and biogeochemical point data are from the GLODAPv2 data set (https://www.nodc.noaa.gov/ocads/oceans/GLODAPv2/) and the gridded modern $\delta^{13}C_{DIC}$ subsurface field is from the Eide, Olsen, Ninnemann, Eldevik, and Johannessen, 2017 repository. Model output at monthly frequency can be accessed via this site https://doi.org/10.5281/zenodo.4458981.

References

Adcroft, A., Anderson, W., Balaji, V., Blanton, C., Bushuk, M., Dufour, C. O., et al. (2019). The GFDL global ocean and sea ice model OM4.0: Model description and simulation features. *Journal of Advances in Modeling Earth Systems*, *11*(10), 3167–3211. https://doi.org/10.1029/2019MS001726

Anderson, L. A., & Sarmiento, J. L. (1994). Redfield ratios of remineralization determined by nutrient data analysis. *Global Biogeochemical Cycles*, *8*(1), 65–80. https://doi.org/10.1029/93GB03318

Becker, M., Andersen, N., Erlenkeuser, H., Humphreys, M. P., Tanhua, T., & Körtzinger, A. (2016). An internally consistent dataset of δ^{13}C-DIC in the north Atlantic Ocean – NAC13v1. *Earth System Science Data*, *8*(2), 559–570. https://doi.org/10.5194/essd-8-559-2016

Becker, M., Steinhoff, T., & Körtzinger, A. (2018). A detailed view on the seasonality of stable carbon isotopes across the north Atlantic. *Global Biogeochemical Cycles*, *32*(9), 1406–1419. https://doi.org/10.1029/2018GB005905

Bernardello, R., Marinov, I., Palter, J. B., Sarmiento, J. L., Galbraith, E. D., & Slater, R. D. (2014). Response of the ocean natural carbon storage to projected twenty-first-century climate change. *Journal of Climate*, *27*(5), 2033–2053. https://doi.org/10.1175/JCLI-D-13-00343.1

Bonneau, M., Vergnaudgrazzini, C., & Berger, W. (1980). Stable isotope fractionation and differential dissolution in recent planktonic-foraminifera from Pacific box-cores. *Oceanologica Acta*, *3*(3), 377–382.

Broecker, W. S. (1974). "NO", a conservative water-mass tracer. *Earth and Planetary Science Letters*, *23*(1), 100–107. https://doi.org/10.1016/0012-821X(74)90036-3

Broecker, W. S., & Maier-Reimer, E. (1992). The influence of air and sea exchange on the carbon isotope distribution in the sea. *Global Biogeochemical Cycles*, *6*(3), 315–320. https://doi.org/10.1029/92GB01672

Broecker, W. S., Peacock, S. L., Walker, S., Weiss, R., Fahrbach, E., Schroeder, M., et al. (1998). How much deep water is formed in the Southern Ocean? *Journal of Geophysical Research*, *103*(C8), 15833–15843. https://doi.org/10.1029/98JC00248

Buckley, M. W., & Marshall, J. (2016). Observations, inferences, and mechanisms of the Atlantic Meridional Overturning Circulation: A review. *Reviews of Geophysics*, *54*(1), 5–63. https://doi.org/10.1002/2015RG000493

Carr, M.-E., Friedrichs, M. A., Schmeltz, M., Aita, M. N., Antoine, D., Arrigo, K. R., et al. (2006). A comparison of global estimates of marine primary production from ocean color. *Deep Sea Research Part II: Topical Studies in Oceanography*, *53*(5), 741–770. https://doi.org/10.1016/j.dsr2.2006.01.028

Charles, C. D., Wright, J. D., & Fairbanks, R. G. (1993). Thermodynamic influences on the marine carbon isotope record. *Paleoceanography*, *8*(6), 691–697. https://doi.org/10.1029/93PA01803

Curry, W. B., & Oppo, D. W. (2005). Glacial water mass geometry and the distribution of δ^{13}C of $\sum CO_2$ in the western Atlantic Ocean. *Paleoceanography*, *20*(1). https://doi.org/10.1029/2004PA001021

Dai, A., Qian, T., Trenberth, K. E., & Milliman, J. D. (2009). Changes in continental freshwater discharge from 1948 to 2004. *Journal of Climate*, *22*(10), 2773–2792. https://doi.org/10.1175/2008JCLI2592.1

Dunne, J. P., Armstrong, R. A., Gnanadesikan, A., & Sarmiento, J. L. (2005). Empirical and mechanistic models for the particle export ratio. *Global Biogeochemical Cycles*, *19*(4). https://doi.org/10.1029/2004GB002390

Dunne, J. P., Hales, B., & Toggweiler, J. R. (2012). Global calcite cycling constrained by sediment preservation controls. *Global Biogeochemical Cycles*, *26*(3), GB3023. https://doi.org/10.1029/2010GB003935

Dunne, J. P., John, J. G., Adcroft, A. J., Griffies, S. M., Hallberg, R. W., Shevliakova, E., et al. (2012). GFDL's ESM2 global coupled climate-carbon earth system models. Part I: Physical formulation and baseline simulation characteristics. *Journal of Climate*, *25*(19), 6646–6665. https://doi.org/10.1175/JCLI-D-11-00560.1

Dunne, J. P., John, J. G., Shevliakova, E., Stouffer, R. J., Krasting, J. P., Malyshev, S. L., et al. (2013). GFDL's ESM2 global coupled climate-carbon earth system models. Part II: Carbon system formulation and baseline simulation characteristics. *Journal of Climate*, *26*(7), 2247–2267. https://doi.org/10.1175/JCLI-D-12-00150.1

Dunne, J. P., Sarmiento, J. L., & Gnanadesikan, A. (2007). A synthesis of global particle export from the surface ocean and cycling through the ocean interior and on the seafloor. *Global Biogeochemical Cycles*, *21*(4). https://doi.org/10.1029/2006GB002907

Duplessy, J. C., Shackleton, N. J., Fairbanks, R. G., Labeyrie, L., Oppo, D., & Kallel, N. (1988). Deepwater source variations during the last climatic cycle and their impact on the global deepwater circulation. *Paleoceanography*, *3*(3), 343–360. https://doi.org/10.1029/PA003i003p00343

Eide, M., Olsen, A., Ninnemann, U. S., & Eldevik, T. (2017). A global estimate of the full oceanic ^{13}C Suess effect since the preindustrial. *Global Biogeochemical Cycles*, *31*(3), 492–514. https://doi.org/10.1002/2016GB005472

Eide, M., Olsen, A., Ninnemann, U. S., Eldevik, T., & Johannessen, T. (2017). Climatological distributions of δ^{13}C of dissolved inorganic carbon in the global oceans [data set]. *PANGAEA*. https://doi.org/10.1594/PANGAEA.872004

Eide, M., Olsen, A., Ninnemann, U. S., & Johannessen, T. (2017). A global ocean climatology of preindustrial and modern ocean δ^{13}C. *Global Biogeochemical Cycles*, *31*(3), 515–534. https://doi.org/10.1002/2016GB005473

Fine, R. A., Maillet, K. A., Sullivan, K. F., & Willey, D. (2001). Circulation and ventilation flux of the Pacific Ocean. *Journal of Geophysical Research*, *106*(C10), 22159–22178. https://doi.org/10.1029/1999JC000184

Francey, R. J., Allison, C. E., Etheridge, D. M., Trudinger, C. M., Enting, I. G., Leuenberger, M., et al. (1999). A 1000-year high precision record of δ^{13}C in atmospheric CO_2. *Tellus B: Chemical and Physical Meteorology*, *51*(2), 170–193. https://doi.org/10.3402/tellusb.v51i2.16269

Galbraith, E. D., Dunne, J. P., Gnanadesikan, A., Slater, R. D., Sarmiento, J. L., Dufour, C. O., et al. (2015). Complex functionality with minimal computation: Promise and pitfalls of reduced-tracer ocean biogeochemistry models. *Journal of Advances in Modeling Earth Systems*, *7*(4), 2012–2028. https://doi.org/10.1002/2015MS000463

Galbraith, E. D., Gnanadesikan, A., Dunne, J. P., & Hiscock, M. R. (2010). Regional impacts of iron-light colimitation in a global biogeochemical model. *Biogeosciences*, *7*(3), 1043–1064. https://doi.org/10.5194/bg-7-1043-2010

Goericke, R., & Fry, B. (1994). Variations of marine plankton δ^{13}C with latitude, temperature, and dissolved CO_2 in the world ocean. *Global Biogeochemical Cycles*, *8*(1), 85–90. https://doi.org/10.1029/93GB03272

Griffies, S. M. (2012a). *Elements of the Modular Ocean Model (MOM) (2012 release with updates) (NOAA GFDL ocean group technical report No. 7)*. Retrieved from http://www.mom-ocean.org/web/docs/project/MOM5elements.pdf

Griffies, S. M. (2012b). *A suite of coupled model test cases. Techical report*.

Griffies, S. M., Biastoch, A., Böning, C., Bryan, F., Danabasoglu, G., Chassignet, E. P., et al. (2009). Coordinated Ocean-ice Reference Experiments (COREs). *Ocean Modelling*, *26*(1), 1–46. https://doi.org/10.1016/j.ocemod.2008.08.007

Heuzé, C., Heywood, K. J., Stevens, D. P., & Ridley, J. K. (2013). Southern Ocean bottom water characteristics in CMIP5 models. *Geophysical Research Letters*, *40*(7), 1409–1414. https://doi.org/10.1002/grl.50287

Hilting, A. K., Kump, L. R., & Bralower, T. J. (2008). Variations in the oceanic vertical carbon isotope gradient and their implications for the Paleocene-Eocene biological pump. *Paleoceanography*, *23*(3). https://doi.org/10.1029/2007PA001458

Ho, D. T., Law, C. S., Smith, M. J., Schlosser, P., Harvey, M., & Hill, P. (2006). Measurements of air-sea gas exchange at high wind speeds in the Southern Ocean: Implications for global parameterizations. *Geophysical Research Letters*, *33*(16). https://doi.org/10.1029/2006GL026817

Holden, P. B., Edwards, N. R., Müller, S. A., Oliver, K. I. C., Death, R. M., & Ridgwell, A. (2013). Controls on the spatial distribution of oceanic $\delta^{13}C_{DIC}$. *Biogeosciences*, *10*(3), 1815–1833. https://doi.org/10.5194/bg-10-1815-2013

Jacobson, A. R., Mikaloff Fletcher, S. E., Gruber, N., Sarmiento, J. L., & Gloor, M. (2007). A joint atmosphere-ocean inversion for surface fluxes of carbon dioxide: 1. Methods and global-scale fluxes. *Global Biogeochemical Cycles*, *21*(1). https://doi.org/10.1029/2005GB002556

Jahn, A., Lindsay, K., Giraud, X., Gruber, N., Otto-Bliesner, B. L., Liu, Z., & Brady, E. C. (2015). Carbon isotopes in the ocean model of the Community Earth System Model (CESM1). *Geoscientific Model Development*, *8*(8), 2419–2434. https://doi.org/10.5194/gmd-8-2419-2015

Keir, R., Rehder, G., Suess, E., & Erlenkeuser, H. (1998). The δ^{13}C anomaly in the northeastern Atlantic. *Global Biogeochemical Cycles*, *12*(3), 467–477. https://doi.org/10.1029/98GB02054

Keller, K., & Morel, F. M. M. (1999). A model of carbon isotopic fractionation and active carbon uptake in phytoplankton. *Marine Ecology Progress Series*, *182*, 295–298. https://doi.org/10.3354/meps182295

Ko, Y. H., Lee, K., Quay, P. D., & Feely, R. A. (2014). Decadal (1994-2008) change in the carbon isotope ratio in the eastern south Pacific Ocean. *Global Biogeochemical Cycles*, *28*(8), 775–785. https://doi.org/10.1002/2013GB004786

Large, W. G., & Yeager, S. (2004). *Diurnal to decadal global forcing for ocean and sea-ice models: The data sets and flux climatologies*. NCAR Technical Note NCAR/TN-460+STR.

Laws, E. A., Popp, B. N., Bidigare, R. R., Kennicutt, M. C., & Macko, S. A. (1995). Dependence of phytoplankton carbon isotopic composition on growth rate and $[CO_2]_{aq}$: Theoretical considerations and experimental results. *Geochimica et Cosmochimica Acta*, *59*(6), 1131–1138. https://doi.org/10.1016/0016-7037(95)00030-4

Lisiecki, L. E. (2010). A benthic δ^{13}C-based proxy for atmospheric pCO₂ over the last 1.5 Myr. *Geophysical Research Letters*, *37*(21). https://doi.org/10.1029/2010GL045109

Lynch-Stieglitz, J., Stocker, T. F., Broecker, W. S., & Fairbanks, R. G. (1995). The influence of air-sea exchange on the isotopic composition of oceanic carbon: Observations and modeling. *Global Biogeochemical Cycles*, *9*(4), 653–665. https://doi.org/10.1029/95GB02574

Morée, A. L., Schwinger, J., & Heinze, C. (2018). Southern Ocean controls of the vertical marine δ^{13}C gradient – a modeling study. *Biogeosciences*, *15*(23), 7205–7223. https://doi.org/10.5194/bg-15-7205-2018

Muller-Karger, F., McClain, C. R., & Richardson, P. L. (1988). The dispersal of the Amazon's water. *Nature*, *333*, 5659. https://doi.org/10.1038/333056a0

Murnane, R. J., & Sarmiento, J. L. (2000). Roles of biology and gas exchange in determining the δ^{13}C distribution in the ocean and the preindustrial gradient in atmospheric δ^{13}C. *Global Biogeochemical Cycles*, *14*(1), 389–405. https://doi.org/10.1029/1998GB001071

Najjar, R., & Orr, J. C. (1998). *Design of OCMIP-2 simulations of chlorofluorocarbons, the solubility pump and common biogeochemistry (LSCE/CEASaclay internal OCMIP report)*.

Nightingale, P. D., Malin, G., Law, C. S., Watson, A. J., Liss, P. S., Liddicoat, M. I., et al. (2000). In situ evaluation of air-sea gas exchange parameterizations using novel conservative and volatile tracers. *Global Biogeochemical Cycles*, *14*(1), 373–387. https://doi.org/10.1029/1999gb900091

Olsen, A., Lange, N., Key, R. M., Tanhua, T., Bittig, H. C., Kozyr, A., et al. (2020). An updated version of the global interior ocean biogeochemical data product, GLODAPv2.2020. *Earth System Science Data*, *12*(4), 3653–3678. https://doi.org/10.5194/essd-12-3653-2020

Olsen, A., & Ninnemann, U. (2010). Large δ^{13}C gradients in the preindustrial north atlantic revealed. *Science*, *330*(6004), 658–659. https://doi.org/10.1126/science.1193769

Orr, J. C., Najjar, R. G., Aumont, O., Bopp, L., Bullister, J. L., Danabasoglu, G., et al. (2017). Biogeochemical protocols and diagnostics for the CMIP6 ocean model intercomparison project (OMIP). *Geoscientific Model Development*, *10*(6), 2169–2199. https://doi.org/10.5194/gmd-10-2169-2017

Popp, B. N., Takigiku, R., Hayes, J. M., Louda, J. W., & Baker, E. W. (1989). The post-paleozoic chronology and mechanism of ^{13}C depletion in primary marine organic-matter. *American Journal of Science*, *289*, 436–454. https://doi.org/10.2475/ajs.289.4.436

Quay, P., Sonnerup, R., Munro, D., & Sweeney, C. (2017). Anthropogenic CO_2 accumulation and uptake rates in the Pacific Ocean based on changes in the ^{13}C/^{12}C of dissolved inorganic carbon. *Global Biogeochemical Cycles*, *31*(1), 59–80. https://doi.org/10.1002/2016GB005460

Quay, P., Sonnerup, R., Stutsman, J., Maurer, J., Körtzinger, A., Padin, X. A., & Robinson, C. (2007). Anthropogenic CO_2 accumulation rates in the North Atlantic Ocean from changes in the ^{13}C/^{12}C of dissolved inorganic carbon. *Global Biogeochemical Cycles*, *21*(1). https://doi.org/10.1029/2006GB002761

Quay, P., Sonnerup, R., Westby, T., Stutsman, J., & McNichol, A. (2003). Changes in the ^{13}C/^{12}C of dissolved inorganic carbon in the ocean as a tracer of anthropogenic CO_2 uptake. *Global Biogeochemical Cycles*, *17*(1), 4–1. https://doi.org/10.1029/2001GB001817

Quay, P., Tilbrook, B., & Wong, C. S. (1992). Oceanic uptake of fossil fuel CO_2: Carbon-13 evidence. *Science*, *256*(5053), 74–79. https://doi.org/10.1126/science.256.5053.74

Sallée, J.-B., Shuckburgh, E., Bruneau, N., Meijers, A. J. S., Bracegirdle, T. J., Wang, Z., & Roy, T. (2013). Assessment of Southern Ocean water mass circulation and characteristics in CMIP5 models: Historical bias and forcing response. *Journal of Geophysical Research: Oceans*, *118*(4), 1830–1844. https://doi.org/10.1002/jgrc.20135

Sarmiento, J., & Gruber, N. (2006). *Ocean biogeochemical dynamics*. Princeton University Press.

Sarmiento, J., & Sundquist, E. (1992). Revised budget for the oceanic uptake of anthropogenic carbon dioxide. *Nature*, *356*, 589–593. https://doi.org/10.1038/356589a0

Schmidtko, S., Stramma, L., & Visbeck, M. (2017). Decline in global oceanic oxygen content during the past five decades. *Nature*, *542*, 335–339. https://doi.org/10.1038/nature21399

Schmittner, A., Gruber, N., Mix, A. C., Key, R. M., Tagliabue, A., & Westberry, T. K. (2013). Biology and air-sea gas exchange controls on the distribution of carbon isotope ratios (δ^{13}C) in the ocean. *Biogeosciences*, *10*(9), 5793–5816. https://doi.org/10.5194/bg-10-5793-2013

Sonnerup, R. E., Mecking, S., Bullister, J. L., & Warner, M. J. (2015). Transit time distributions and oxygen utilization rates from chlorofluorocarbons and sulfur hexafluoride in the Southeast Pacific Ocean. *Journal of Geophysical Research: Oceans*, *120*(5), 3761–3776. https://doi.org/10.1002/2015JC010781

Sonnerup, R. E., & Quay, P. D. (2012). ^{13}C constraints on ocean carbon cycle models. *Global Biogeochemical Cycles*, *26*(2). https://doi.org/10.1029/2010GB003980

Sonnerup, R. E., Quay, P. D., McNichol, A. P., Bullister, J. L., Westby, T. A., & Anderson, H. L. (1999). Reconstructing the oceanic ^{13}C Suess effect. *Global Biogeochemical Cycles*, *13*(4), 857–872. https://doi.org/10.1029/1999GB900027

Sweeney, C., Gloor, E., Jacobson, A. R., Key, R. M., McKinley, G., Sarmiento, J. L., & Wanninkhof, R. (2007). Constraining global air-sea gas exchange for CO_2 with recent bomb ^{14}C measurements. *Global Biogeochemical Cycles*, *21*(2). https://doi.org/10.1029/2006GB002784

Tagliabue, A., & Bopp, L. (2008). Toward understanding global variability in ocean carbon-13. *Global Biogeochemical Cycles*, *22*(1). https://doi.org/10.1029/2007GB003037

Talley, L. D. (2013). Closure of the global overturning circulation through the Indian, Pacific, and Southern oceans: Schematics and transports. *Oceanography*, *26*. https://doi.org/10.5670/oceanog.2013.07

Tans, P. P., Berry, J. A., & Keeling, R. F. (1993). Oceanic ^{13}C/^{12}C observations: A new window on ocean CO_2 uptake. *Global Biogeochemical Cycles*, *7*(2), 353–368. https://doi.org/10.1029/93GB00053

Thyng, K. M., Greene, C. A., Hetland, R. D., Zimmerle, H. M., & DiMarco, S. F. (2016). True colors of oceanography: Guidelines for effective and accurate colormap selection. *Oceanography*, *29*(3), 9–13. https://doi.org/10.5670/oceanog.2016.66

Toggweiler, J. R., Dixon, K., & Bryan, K. (1989). Simulations of radiocarbon in a coarse-resolution world ocean model: 2. Distributions of bomb-produced carbon 14. *Journal of Geophysical Research*, *94*(C6), 8243–8264. https://doi.org/10.1029/JC094iC06p08243

Trull, T., & Armand, L. (2001). Insights into southern ocean carbon export from the δ^{13}C of particles and dissolved inorganic carbon during the SOIREE iron release experiment. *Deep Sea Research Part II: Topical Studies in Oceanography*, *48*(11), 2655–2680. https://doi.org/10.1016/S0967-0645(01)00013-3

Wanninkhof, R. (1992). Relationship between wind speed and gas exchange over the ocean. *Journal of Geophysical Research*, *97*(C5), 7373–7382. https://doi.org/10.1029/92JC00188

Wanninkhof, R. (2014). Relationship between wind speed and gas exchange over the ocean revisited. *Limnology and Oceanography: Methods*, *12*(6), 351–362. https://doi.org/10.1016/j.jastp.2013.12.009

Zhang, J., Quay, P., & Wilbur, D. (1995). Carbon isotope fractionation during gas-water exchange and dissolution of CO_2. *Geochimica et Cosmochimica Acta*, *59*(1), 107–114. https://doi.org/10.1016/0016-7037(95)91550-D